

Thin-Walled Structures

Analytical and Finite Element Analyses on Axial Tensile Behavior of Origami Bellows with Polygonal Cross-Section

--Manuscript Draft--

Manuscript Number:	TWST-D-23-01876
Article Type:	Research Paper
Section/Category:	Tubular structures
Keywords:	Origami bellows; energy absorption; basic deployment element; axial tension
Manuscript Region of Origin:	Asia Pacific
Abstract:	The mechanical behavior and energy absorption of origami bellows with polygonal cross-section under quasi-static axial tension were numerically and theoretically investigated. The finite element results showed that the plateau force increased with the number of polygonal sides N, leading to an enhancement in both the mean tensile force (Pm) and the specific energy absorption (SEA) by 22.05% and 23.85%, respectively, when N increased from 5 to 8. Two types of basic deployment elements during the tensile process of hexagonal cross-section bellows were defined in two deployment modes, namely non-rigid deployment mode I and non-rigid deployment mode II. The bellows which deployed in the latter mode showed approximately 60% improvement in both SEA and Pm compared with their counterparts deployed in the former mode. Theoretical predictions of the mean tensile force for each mode were derived based on a rigid-perfectly plastic analysis with super folding elements. The predicted results showed a reasonable agreement with the finite element results in terms of the force-displacement history and mean tensile force. This work reveals the fundamental mechanics involved and can facilitate design of origami bellows with optimized geometric and material parameters for desired energy absorption behavior.

- Tensile behavior of origami bellows with polygonal cross-section was investigated.
- The energy absorption of the bellows increased with the number of polygonal sides.
- Two types of non-rigid deployment modes were discovered.
- Analytical model of mean tensile force for each deployment mode was derived.
- The predicted results were validated against numerical results.

Analytical and Finite Element Analyses on Axial Tensile Behavior of Origami Bellows with Polygonal Cross-Section

Xinyi Zhang¹ Dora Karagiozova², Guoxing Lu^{1,*}, Yvonne Durandet¹, Shenghai Wang³

¹ School of Engineering, Swinburne University of Technology, Hawthorn, Vic 3122, Australia

² Institute of Mechanics, Bulgarian Academy of Sciences, Acad. G. Bonchev St., Block 4, Sofia 1113, Bulgaria

³ School of Mechanical, Electrical & Information Engineering, Shandong University (Weihai), Weihai 264209, China

Abstract

The mechanical behavior and energy absorption of origami bellows with polygonal cross-section under quasi-static axial tension were numerically and theoretically investigated. The finite element results showed that the plateau force increased with the number of polygonal sides N , leading to an enhancement in both the mean tensile force (P_m) and the specific energy absorption (SEA) by 22.05% and 23.85%, respectively, when N increased from 5 to 8. Two types of basic deployment elements during the tensile process of hexagonal cross-section bellows were defined in two deployment modes, namely non-rigid deployment mode I and non-rigid deployment mode II. The bellows which deployed in the latter mode showed approximately 60% improvement in both SEA and P_m compared with their counterparts deployed in the former mode. Theoretical predictions of the mean tensile force for each mode were derived based on a rigid-perfectly plastic analysis with super folding elements. The predicted results showed a reasonable agreement with the finite element results in terms of the force-displacement history and mean tensile force. This work reveals the fundamental mechanics involved and can facilitate design of origami bellows with optimized geometric and material parameters for desired energy absorption behavior.

Keywords: Origami bellows; energy absorption; basic deployment element; axial tension.

1 Introduction

Thin-walled structures have become increasingly popular in transportation such as automobiles, trains, and aircraft due to their lightweight, cost-effectiveness and high efficiency [1]. They have also proven to be effective as energy dissipation components in protecting both people and cargo from collisions. During an impact, the kinetic energy of the collision is effectively converted into plastic energy by deforming the structure under axial loading [1]. This helps to dissipate the impact energy and mitigate the damage caused by the collision [2]. Among energy absorbers, conventional thin-walled tubes have received significant attention from researchers due to their simple structures, long-stroke distance, high mean force, and high specific energy absorption (*SEA*) [3].

In practice, a smooth crushing process and a low initial peak force are two important indicators for a high-performance thin-walled tube under collapse deformation [1]. However, a conventional thin-walled tube under axial compressive loading has a high initial peak force corresponding to the onset of buckling followed by fluctuations, which leads to a low efficiency in energy absorption [4]. A large number of studies have focused on modifying the geometric parameters of conventional thin-walled tubes in order to improve their energy absorption performance; they include the multi-cell tubes [5-7], corrugated tubes [8-10] and tapered tubes [11, 12]. Moreover, varying material properties such as strength, ductility and density contribute to the energy absorption capacity of the thin-walled tubes. Various materials have been studied, such as metals [13, 14], polymers and composites [15-17].

Rigid origami pattern involves plastic bending along folding lines, which are stationary of a fixed length. However, facets also bend in a non-rigid origami and this leads to traveling plastic hinges, which may dissipate more energy. Therefore, to improve energy absorption performance of thin-walled tubes, efforts have been made to increase folding lines. Changing the number of sides, N , of the tubes could introduce more folding lines and modules into

tubes. Rossi et al. [18] numerically investigated the dynamic behavior of conventional tubes with polygonal cross-section. It was revealed that the mean crushing force was significantly impacted by N . Song et al. [4] proposed equilateral trapezoid patterned tubes with different cross-sections, where $N = 4, 6, 8$. The results showed that a smoother force response and lower initial peak force were obtained compared with conventional tubes. Nia et al. [19] experimentally and numerically investigated the quasi-static crushing process and energy absorption performance of thin-walled tubes with various N ranging from three to eight. They found that the uniform polygonal tube with a smaller value of N showed less energy absorption. Both quasi-static and dynamic behavior of various polygonal tubes were investigated by Yamashita et al. [20]. It was concluded that the crushing strength increased with N but it reached a point of near saturation when N exceeded six. In addition to the tubes with common polygonal cross-sections, some tubes with various structurally designed cross-sections have been proposed to improve deformation process and energy absorption of tubes, such as tubes with star-shaped cross-section[21], bionic-bamboo tubes with six different cross-section [22], multicell tubes with hierarchical structures [23, 24].

The analytical solution the average crushing force has been developed based on the deformation modes of circular and square tubes under axial crushing. Alexander [25] firstly proposed a model of mean crushing force for a circular tube that deformed in the ring mode. In his study, the collapse folds were assumed to be fully external and flattened. Abramowicz and Jones [26] later revised the analytical model of the average force by involving the curvature part of the folds into the model. Wierzbicki et al. [27] considered both internal and external folds into the model to obtain more accurate model than those in the previous studies. Recently, Lu et al. [28] have proposed a new collapse mechanism including both inwards and outwards folding walls of the tube. This approach could give the mean crushing force and the corresponding force-displacement curve as well as plastic folding length of the

1 large plastic deformation of the circular tube subjected to axial crushing. A deformation
2 mechanism of thin square tubes was described by Wierzbicki and Abramowicz as a super
3 folding element, including stationary plastic lines, moving plastic hinge lines and toroidal
4 surface [29]. They proposed an analytical model for the mean crushing force. Subsequently,
5 Abramowicz and Włodzimierz [30] improved the model by considering an effective crushing
6 distance instead of the total length of the tube. This theory is extensively used to predict the
7 mean force of thin-walled tubes under compression [31-33].
8
9

10 Recently, a series of thin-walled tubes with origami patterns have been proposed to
11 improve their energy absorption [34-36]. They offer two new features. First, the origami tube
12 can be fabricated by folding a 2D (two-dimension) surface into a 3D (three-dimension)
13 configuration. The flexible designing of the pattern provides desirable mechanical
14 characteristics. Second, the pre-designed patterns on the surface of the tube can effectively
15 trigger a high-performance collapse mode under crushing, resulting in more material
16 destroys to enhance the energy absorption capacity of the tube [37]. The initial peak force and
17 the mechanical process can also be controlled by crushing the pre-designed pattern. For
18 instance, Song et al. [4] examined the deformation and energy absorption characteristics of
19 thin-walled tubes with equilateral trapezoid patterns under axial crushing. They found a more
20 uniform crushing process and a significant decrease in initial peak force by 35%-76%, when
21 compared with a conventional tube. Later, Ma and You [38] proposed a group of square
22 origami crash boxes with full diamond pattern and found a higher mean crushing force and
23 more uniform force due to more and longer travelling plastic hinges invoked, compared with
24 the straight tube. Recently, Liu et al. [39] have introduced curved Miura origami pattern into
25 an octagon tube and found that the global buckling could be suppressed with a maximum
26 reduction of 59.9% in the magnitude of lateral deformation.
27
28
29
30
31
32
33
34
35
36
37
38
39
40
41
42
43
44
45
46
47
48
49
50
51
52
53
54
55
56
57
58
59
60
61
62
63
64
65

Origami bellows have been shown to exhibit deployment behaviour when subjected to external loading [40-42] and can find wide applications. Their deformation process is determined by geometric compatibility and can be divided into two categories: rigid deformation and non-rigid deformation. The latter, as it involves more material in plastic deformation, is a preferred choice for high-performance energy absorption. Sharma and Upadhyay [41] have experimentally demonstrated that origami bellows with conical Miura-ori patterns exhibit non-rigid deployment behaviour which featured both panel buckling and crease distortions. Additionally, more characteristics of origami bellows have been explored, such as reconfigurable characteristics [43] and bistable states. [34, 44, 45].

Origami bellows, as one type of thin-walled bellows, under tension can be widely used in various industries such as structural engineering, aerospace and automotive due to their thin walls and high strength-to-weight ratio. Some specific applications of origami bellows employed as a flexible element in structures where movement or thermal expansion is expected, such as in pipe systems [46], ducts expansion joints [47], in seismic isolation [48] and vibration damping systems [49]. These origami bellows allow for movement in structures under tension, preventing damage, and also protect underground structures from earthquake ground motion, reducing stress and damage [50]. Additionally, origami bellows are useful as flexible elements in aerospace actuators that can endure tension and movement. With appropriate structural design, these bellows can convert kinetic energy into plastic energy during deformation and prevent damage in tension, resulting in effective energy absorption. Although a significant amount of research has been conducted to understand the mechanical behaviour and energy absorption performance of thin-walled tubes with origami patterns under crushing, sometimes tubes under tension may be applied and there is need to fully comprehend their mechanical modes under tensile loading.

In our previous work, the axial tension behaviour of a thin-walled bellows with pleated origami pattern herein was studied by both the finite element method and experiments [51]. In this paper, an analytical model is developed to predict the mean tensile force of the origami bellows. The mechanical behavior energy absorption of origami bellows with polygonal cross-section subjected to axial tension are studied numerically and theoretically. The layout of the paper is as follows. A detailed geometrical analysis of the origami bellows is given in section 2. Finite element analysis for investigating the effect of polygonal cross-section and deployment modes of origami bellows with hexagonal cross-section under axial quasi-static tension is presented in Section 3. Theoretical investigations on the mechanical response and energy absorption of the origami bellows with hexagonal cross-section are conducted in Section 4. Then, the prediction results are evaluated in terms of force response and mean tensile force in section 5. It is found that the analytical result indicates that the force is proportional to $t^{5/3}$, which explains the empirical relation of $t^{1.67}$ of the previous study [51]. Finally, the conclusion is summarized in Section 6.

2 Geometry

The thin-walled tube constructed by the unit with pleated pattern is named as origami bellows or origami folded cylinders, which can also be found in [52] and [53]. Taking crease pattern of origami bellows with hexagonal cross-section as an example, the dashed lines and solid lines in Fig. 1(a) represent pre-determined valley and mountain creases, respectively. Every folded vertex has four-fold lines denoted with blue and red lines. The flat crease pattern is parameterized by the middle crease length a and b , inclined angle α , unit width $2h$, number of modules M , and number of sides of cross-section N . Fig. 1(b) shows a module of origami bellows generated by folding the patterns along these creases and then joining the two free ends. An origami bellows with a larger number of modules can be built by stacking a

1 number of modules in the axial direction. The completed uniform origami bellows has a pre-
 2 folding angle 2θ , the angle between the adjacent inclined lines in the folded module β , cross-
 3 sectional diameter D , and rotationally symmetric angle 2φ as shown in Fig. 1(b) and (c). The
 4 relationships among the aforementioned geometric parameters are as follows [43]:
 5
 6
 7
 8
 9

$$\sin 2\theta = \cos \varphi \sin \beta \csc^2 \alpha \quad (1)$$

$$D = (a - b) \sec \alpha \cos \left(\frac{\beta}{2} \right) \quad (2)$$

$$\varphi = \frac{\pi}{N} \quad (N \geq 3) \quad (3)$$

$$2\varphi = \pi - 2\alpha' \quad (4)$$

$$D \cos \varphi \sec \theta > 2h \quad (5)$$

27
 28
 29 The crease length a is changed to ensure all models with different polygon cross-sections
 30 have identical surface area. As the number of units along the circumference, N , increases, the
 31 origami bellows would tend to be a circular tube. Here, the models of origami bellows with
 32 different polygonal cross-section are built, as shown in Fig. 1(d).

33 All origami bellows were constructed with six modules and identical areas. The
 34 minimum value of h was set at 5mm to ensure a sufficient area, while origami bellows with h
 35 =12mm were also investigated. The study also considered three typical pre-folding angles
 36 (60° , 70° , and 80°) and three wall thicknesses (0.2mm, 0.3mm, and 0.4mm). A total number
 37 of eighteen finite element models were constructed, and their geometries are summarized in
 38 Table 1. The notation PEN/HEX/HEP/OCT- 2θ - h - t is adopted to name the polygonal cross-
 39 section origami bellows with different geometric parameters, in which PEN, HEX, HEP and
 40 OCT respectively represent pentagonal, hexagonal, heptagonal, and octagonal cross-section.
 41
 42
 43
 44
 45
 46
 47
 48
 49
 50
 51
 52
 53
 54
 55
 56
 57
 58
 59
 60
 61
 62
 63
 64

As an example, OCT-80-12-0.3 denotes a bellows with an octagonal cross-section, a pre-folding angle of 80° , a half unit width of 12mm, and a wall thickness of 0.3mm.

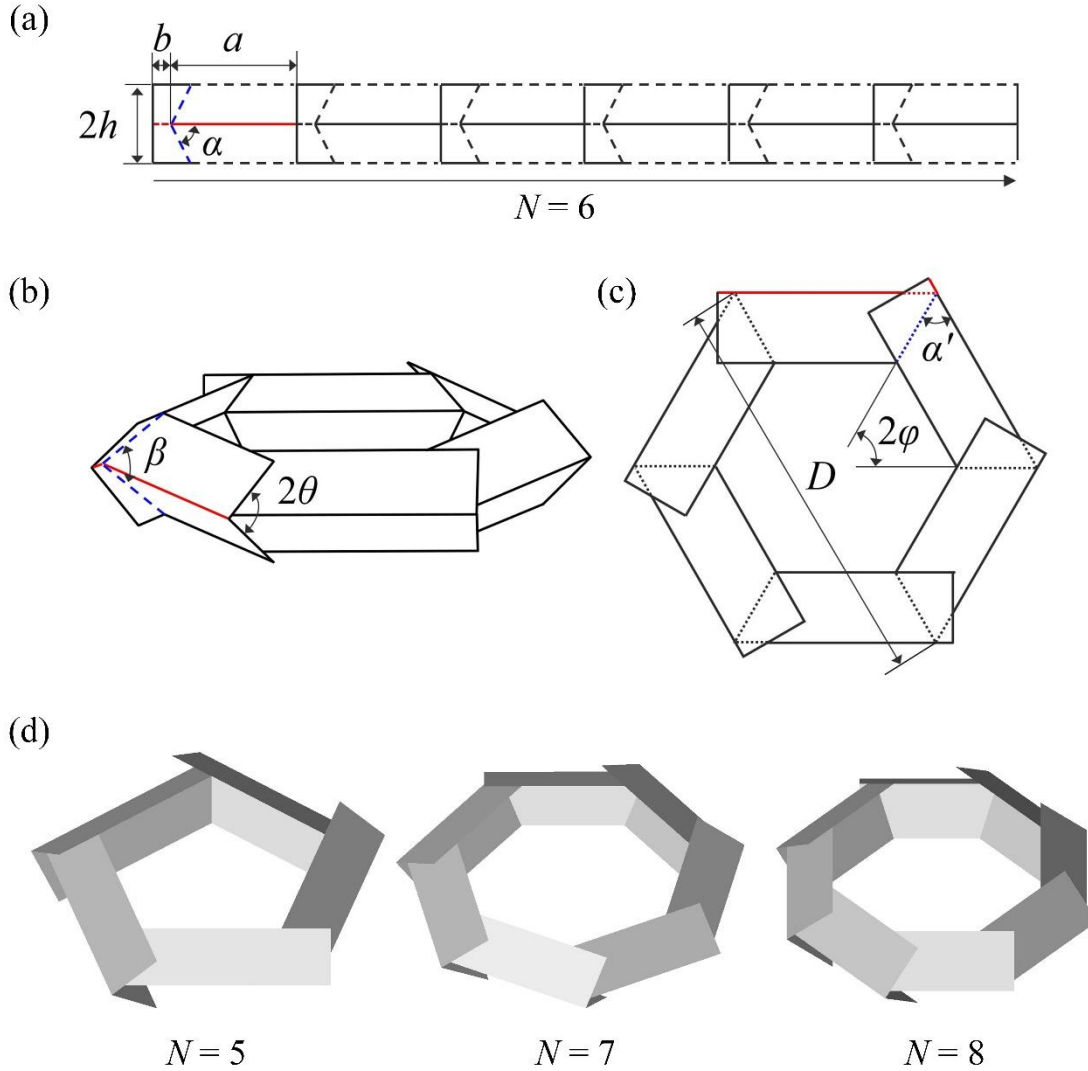


Fig. 1. (a) A flat pleated pattern for one module with hexagonal cross-section. (b) A folded module with hexagonal cross-section. (c) Top view of origami bellows with hexagonal cross-section. (d) A single folded module with pentagonal ($N = 5$), heptagonal ($N = 7$), and octagonal ($N = 8$) cross-section.

3 Finite element analysis

3.1 Modelling

Abaqus/Explicit was adopted to simulate the quasi-static tensile deformation of the origami bellows. The finite element method was used and validated with experiments in [51]. The nodes at the long sides of each unit in the top module moved upwards, while the corresponding nodes in the bottom module were fixed in the loading direction. The nodes in both the ends were constrained in all rotational directions. In addition, the other nodes at the ends were free to deploy.

A loading velocity of 0.3m/s was applied to all the models to avoid dynamic effect. At the same time, the ratio of kinetic energy to internal energy was kept below 5%. To achieve a convergent result, a four-node shell element SR4 with a global size of 0.8mm was used to mesh the model. The material properties of oxide aluminum (Al 1060) obtained from [51] were used assuming an elastic, perfectly-plastic material with density $\rho = 2.7 \times 10^3$ kg/m³, Young's modulus $E = 38.9$ GPa, Poisson's ratio $\nu = 0.3$ and yield stress $\sigma_Y = 62$ MPa.

3.2 FEA Results

3.2.1 Effects of polygonal cross-section

To understand the effects of the number of sides of polygonal cross-section, N , on the mechanical behavior and energy absorption of origami bellows under tension, the deformation process of the bellows with $h = 12$ mm but different N are shown in Fig. 2. It can be seen that the modules deployed asynchronously, regardless of their cross-sectional shape, and stationary plastic hinges formed along the folded lines. The von Mises stress contour indicates that plastic deformation first occurred round the areas surrounding the folded vertices. As the tensile displacement increased, plastic deformation occurred alone the folded lines then gradually developed within the facets. Finally, both fold lines and facets underwent plastic deformation, indicating the bellows with different cross-sections deployed as a non-rigid deployment mode.

1
 2
 3
 4
 5
 6
 7
 8
 9
 10
 11
 12
 13
 14
 15
 16
 17
 18
 19
 20
 21
 22
 23
 24
 25
 26
 27
 28
 29
 30
 31
 32
 33
 34
 35
 36
 37
 38
 39
 40
 41
 42
 43
 44
 45
 46
 47
 48
 49
 50
 51
 52
 53
 54
 55
 56
 57
 58
 59
 60
 61
 62
 63
 64
 65

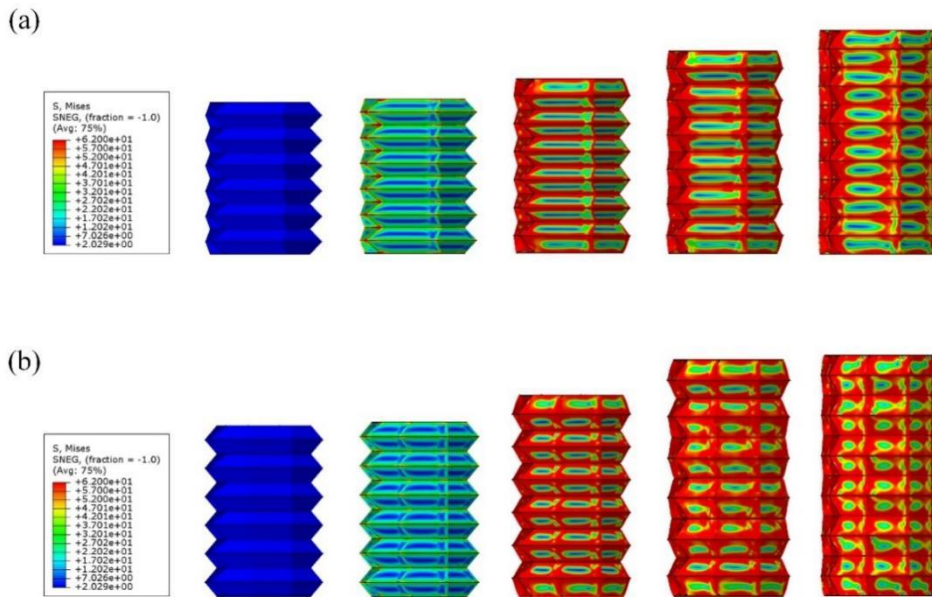


Fig. 2. Tensile deformation process with von Mises stress contours of (a) PEN-80-12-0.3 and (b) OCT-80-12-0.3.

The comparison of tensile force of PEN-80-12-0.3, HEX-80-12-0.3, HEP-80-12-0.3 and OCT-80-12-0.3 is shown in Fig. 3. A smooth curve with no excessive initial peak force can be obtained in all the cases. Moreover, the bellows with a higher number of N had higher force plateaus, indicating that increasing N can improve the energy absorption performance of origami bellows with the same mass.

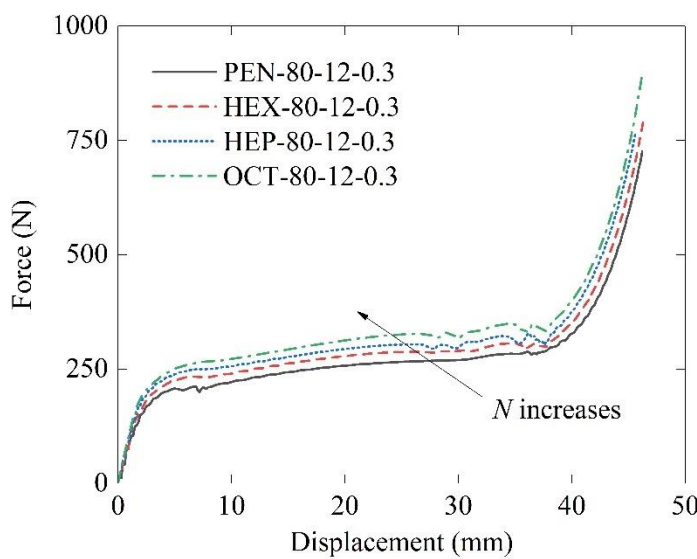


Fig. 3. Force-displacement curves for origami bellows with different polygonal cross-sections ($b = 3\text{mm}$, $h = 12\text{mm}$, $2\theta = 80^\circ$, $M = 6$, $t = 0.3\text{mm}$). N is from 5 to 8.

To evaluate the energy absorption behaviour of the polygonal cross-section bellows, mean tensile force (P_m) and specific energy absorption (SEA) of the bellows were calculated according to the following Eqs. (6) and (7) and plotted in Fig. 4.

$$SEA = \frac{\int_0^{\delta_e} F(\delta) d\delta}{m} \quad (6)$$

where m is the total mass of the origami bellows and δ_e is the effective tensile displacement.

The mean tensile force (P_m) is the average tensile force over the effective tensile distance (δ_e) and it is calculated as:

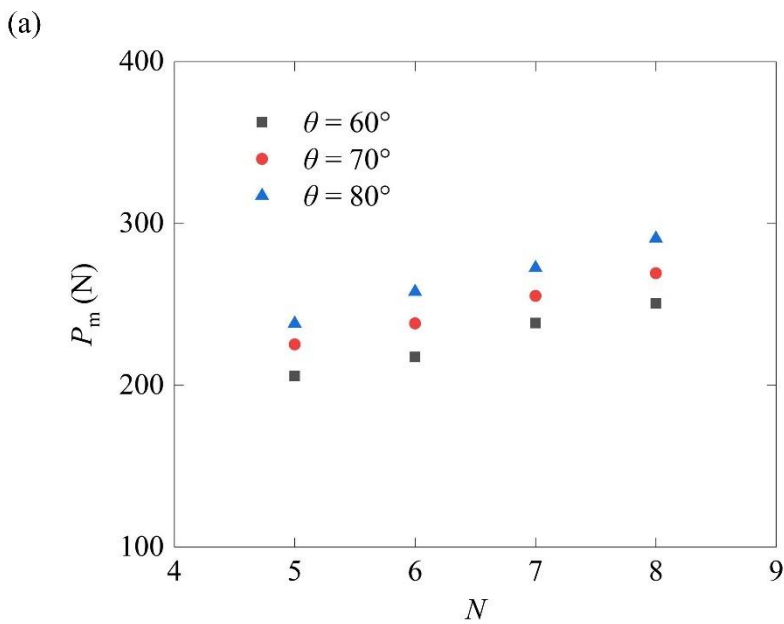
$$P_m = \frac{\int_0^{\delta_e} F(\delta) d\delta}{\delta_e} \quad (7)$$

The energy efficiency factor f is determined by [3]

$$f = \frac{\int_0^{\delta_t} F(\delta) d\delta}{F_{\max}} \quad (8)$$

where F is the tensile force, F_{\max} is the maximum tensile force achieved when the tensile displacement falls within the range of 0 to δ_t .

It can be observed from Fig. 4 that both P_m and SEA increased as N increased, which indicates the bellows with a larger number of polygonal sides have a better performance in energy absorption. OCT-80-12-0.3 exhibits a maximum P_m of 290.78 MPa, which is 22.05% higher compared with PEN-80-12-0.3. Additionally, OCT-60-12-0.3 presents a maximum SEA of $0.43 \text{ J}\cdot\text{g}^{-1}$, representing a 23.85% increase compared to PEN-60-12-0.3.



1
2
3
4
5
6
7
8
9
10
11
12
13
14
15
16
17
18
19
20
21
22
23
24
25
26
27
28
29
30
31
32
33
34
35
36
37
38
39
40
41
42
43
44
45
46
47
48
49
50
51
52
53
54
55
56
57
58
59
60
61
62
63
64
65

(b)

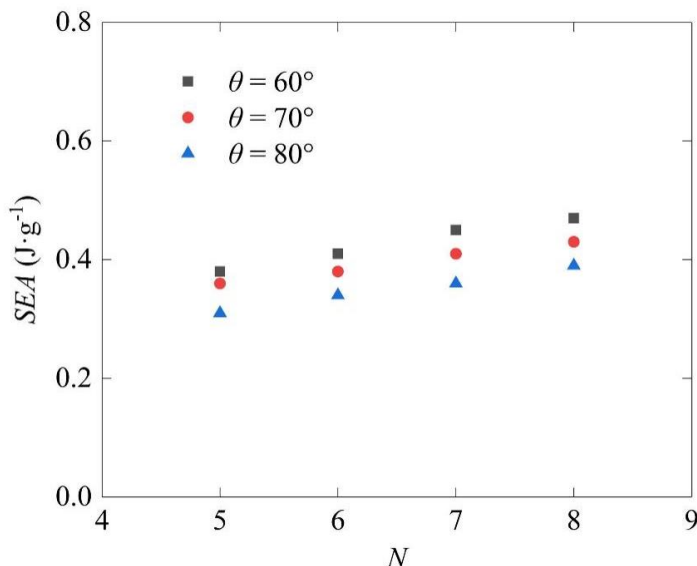


Fig. 4. SEA and P_m of origami bellows with different polygonal cross-sections N and different pre-folding angle 2θ ($h = 12\text{mm}$ and $t = 0.3\text{mm}$).

To understand the deformation mechanisms of the modules in the bellows with different polygonal cross-sections, the Mises stress contours of single module for each fully unfolded unit is presented in Fig. 5. A unit consists of four facets, which are respectively marked as 1, 2, 3 and 4, as shown in Fig. 5(a). It can be observed that all models exhibited stress distribution primarily in the latter sections of facets 3 and 4, accompanied with bending of facets and the formation of creases. However, in the case of PEN-80-12-0.3, the region around the vertex experienced bending without displaying any conspicuous stress distribution. In contrast, the other three bellows displayed plastic deformation near the vertex, as highlighted by the red dashed circles in Fig. 5(b, c, and d). Specifically, HEX-80-12-0.3 showed stress concentration around facets 3 and 4, adjacent to the inclined creases; HEP-80-12-0.3 and OCT-80-12-0.3 exhibited stress contribution at facets 1 and 2. These observations indicate that origami bellows with different polygonal sides possess distinct deformation mechanisms, leading to varied deployment modes. The regions experiencing plastic

1 deformation play a critical role in energy absorption. Hence, understanding the deformation
 2 modes of origami bellows with diverse cross-sections is important. This study aims to
 3 investigate the deformation mode of origami bellows featuring a hexagonal cross-section for
 4 the first time.
 5
 6
 7
 8
 9
 10
 11

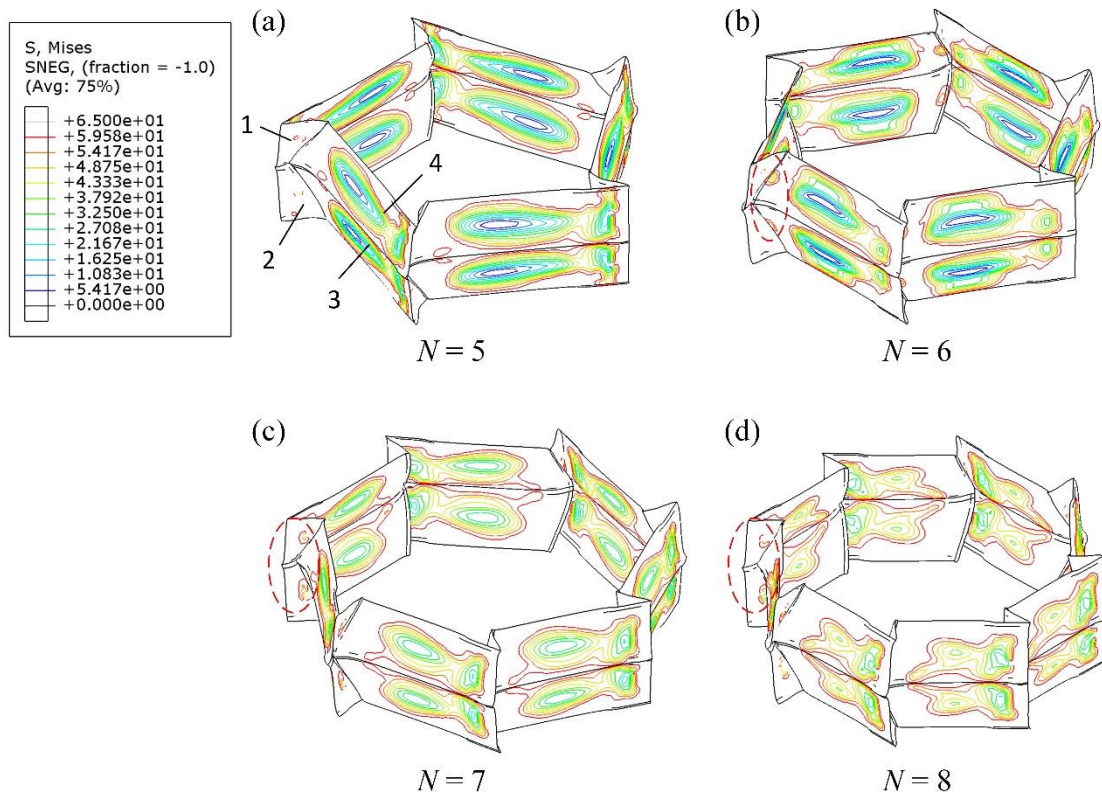


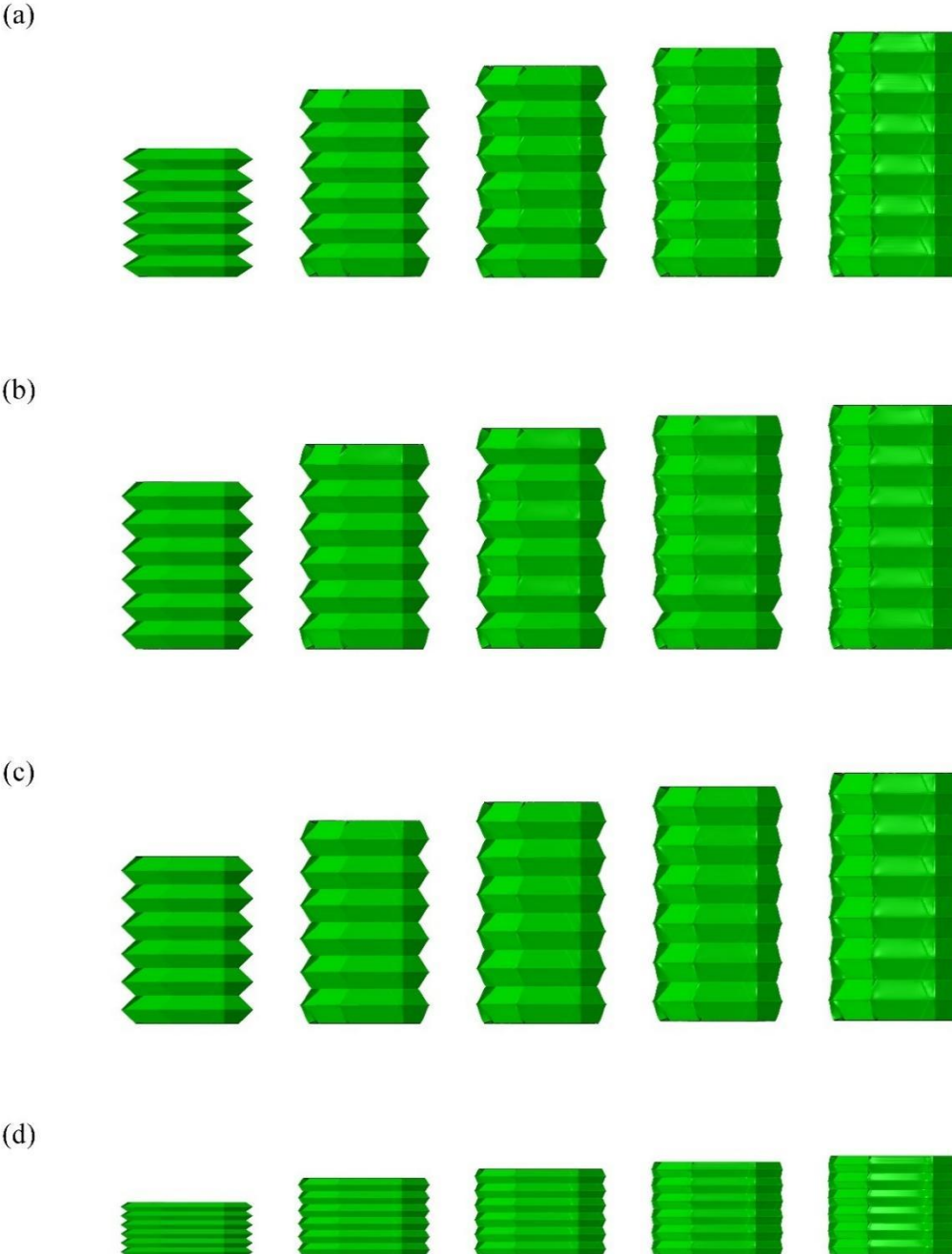
Fig. 5. Mises stress contours of single fully deployed module of (a) PEN-80-12-0.3, (b) HEX-80-12-0.3, (c) HEP-80-12-0.3 and (d) OCT-80-12-0.3.

3.2.2 Deployment modes

To gain a better understanding of the deformation mechanism of origami bellows, the observed types of deformation modes of a hexagonal-sectioned bellows are described here. The tensile progressions of four hexagonal origami bellows with different geometric parameters are shown in Fig. 6. It is observed that all modules of HEX-60-12-0.3 (Fig. 6(a)),

1 except for those at the two boundaries, deformed simultaneously at the initial stage of the
2 tensile process, but then the adjacent areas between two modules experienced randomly
3 outwards displacement. In other words, the deformation of each module was not synchronous.
4
5 This tensile mode with non-rigid asynchronous deployment is hereafter referred to as the
6 *non-rigid deployment mode I*. HEX-70-12-0.3 and HEX-80-12-0.3 were found to deploy in
7 the same mode as HEX-60-12-0.3 with the same h but different θ . For HEX-80-12-0.2, HEX-
8 12-0.3, and HEX-80-12-0.4, with the same h but increasing t , taking (Fig. 6 (b) and (c)) as
9 examples, the tensile progress configurations showed that the outwards deformations of the
10 adjacent areas were also less synchronized, indicating *non-rigid deployment mode I* was
11 involved. Additionally, when t increased, the modules tended to deploy simultaneously, as
12 shown in Fig. 6(c), suggesting a shift in the deformation mode with the increase in t . In
13 contrast, as depicted (Fig. 6 (d)), HEX-60-5-0.3 deployed alone the loading direction, with all
14 modules of the tube deforming simultaneously until it was completely unfolded. The tensile
15 process of HEX-60-5-0.3 was also characterized by non-rigid deploying due to its
16 incompatible geometry. This tensile mode with synchronous deployment is hereafter referred
17 to as the *non-rigid deployment mode II*. This similar tensile process can also be found in
18 HEX-70-5-0.3 and HEX-80-5-0.3. In general, the ratio between half unit width (h) and wall
19 thickness t has a significant effect on the deployment mode of origami bellows. Origami
20 bellows with a large h/t tend to deploy as *non-rigid deployment mode I*, while *non-rigid*
21 *deployment mode II* is more likely to occur in origami bellows with small h/t . More details of
22 these two modes are shown in Fig. 7.

23
24 The numerical results and deployment modes of the origami bellows with hexagonal
25 cross-section are summarized in Table 1. The hexagonal cross-section bellows with wall
26 thickness t of 0.3mm which deployed in non-rigid mode II exhibited approximately a 60%
27 improvement in both SEA and P_m compared with the non-rigid deployment mode I.
28
29
30
31
32
33
34
35
36
37
38
39
40
41
42
43
44
45
46
47
48
49
50
51
52
53
54
55
56
57
58
59
60
61
62
63
64
65



45 **Fig. 6.** Tensile deformation process of (a) HEX-60-12-0.3, (b) HEX-80-12-0.2, (c) HEX-80-
46
47 12-0.4 and (d) HEX-60-5-0.3. The displacements are 64mm, 46mm, 46mm and 26.4mm,
48
49 respectively.
50
51
52
53
54
55
56
57
58
59
60
61
62
63
64
65

1
2
3
4
5
Table 1
67
8
9 Geometries and numerical energy absorption parameters of origami bellows with polygonal
10 cross-sections, as well as their corresponding deployment modes under axial tension.
11
12
13
14
15
16
17
18
19
20
21
22
23
24
25
26
27
28
29
30
31
32
33
34
35
36
37
38
39
40
41
42
43
44
45
46
47
48
49

Model	h (mm)	2θ ($^{\circ}$)	t (mm)	P_m (N)	SEA ($J \cdot g^{-1}$)	Development modes
HEX-80-5-0.2	5	80	0.2	191.43	0.37	II
HEX-60-5-0.3	5	60	0.3	349.58	0.61	II
HEX-70-5-0.3	5	70	0.3	377.62	0.56	II
HEX-80-5-0.3	5	80	0.3	409.85	0.51	II
HEX-60-12-0.3	12	60	0.3	217.47	0.38	I
HEX-70-12-0.3	12	70	0.3	238.28	0.35	I
HEX-80-12-0.3	12	80	0.3	257.80	0.32	I
HEX-80-12-0.2	12	80	0.2	135.62	0.26	I
HEX-80-12-0.4	12	80	0.4	413.09	0.37	I
PEN-60-12-0.3	12	60	0.3	205.76	0.35	-
PEN-70-12-0.3	12	70	0.3	225.33	0.33	-
PEN-80-12-0.3	12	80	0.3	238.24	0.29	-
HEP-60-12-0.3	12	60	0.3	238.49	0.42	-
HEP-70-12-0.3	12	70	0.3	255.32	0.37	-
HEP-80-12-0.3	12	80	0.3	272.61	0.34	-
OCT-60-12-0.3	12	60	0.3	250.56	0.43	-
OCT-70-12-0.3	12	70	0.3	269.26	0.39	-
OCT-80-12-0.3	12	80	0.3	290.78	0.36	-

50
51 To understand the cause of different deformation mechanisms and different modes in
52 origami bellows with different h/t , the equivalent plastic strain (PEEQ) contour map of the
53 deformed configurations of the single module is examined, as shown in Fig. 7. It was
54 observed that the stationary plastic hinges formed along the creases, and the large plastic
55 zones were generated at vertexes of each module. When $h/t = 40$ (e.g. HEX-60-12-0.3), one
56
57
58
59
60
61
62
63
64
65

initially inclined line was transformed into two sub-lines during the tensile deformation.
 1
 These two sub-lines travelled in the opposite directions, as indicated by the yellow arrows in
 2
 Fig. 7(a). This transformation of one pair of inclined hinges into two pairs of traveling plastic
 3
 hinge lines resulted in non-rigid deployment mode I. The travelling plastic hinge lines
 4
 eventually swept to the white dashed lines. Conversely, when h/t decreased to 16.67, one pair
 5
 of traveling plastic hinge lines formed from the initially inclined lines, as depicted in Fig.
 6
 7
 8
 9
 10
 11
 12
 13
 14
 15
 16

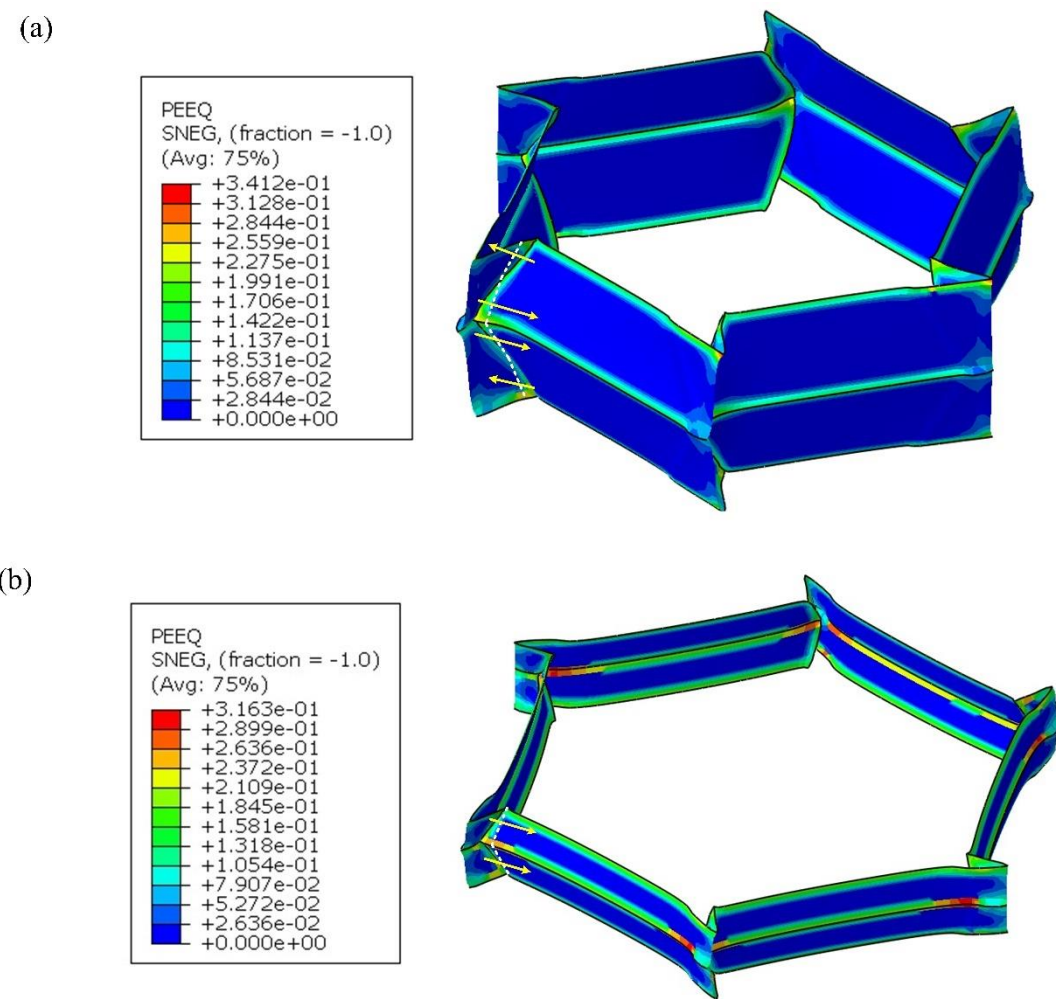


Fig. 7. Equivalent plastic strain contour map of deformed configurations of single module of
 54
 (a) HEX-60-12-0.3 ($h/t = 40$) and (b) HEX-60-5-0.3 ($h/t = 16.67$).
 55
 56
 57
 58
 59
 60
 61
 62
 63
 64
 65

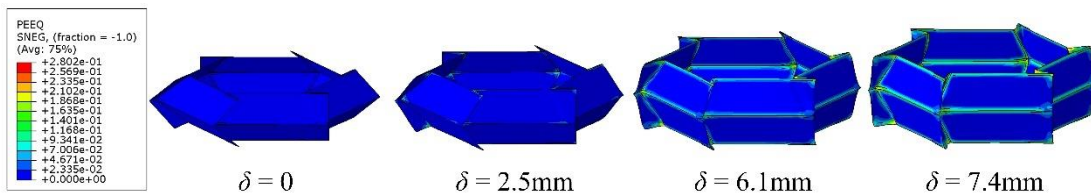
1
2
3
4
5
6
7
8
9
10
11
12
13 **4 Analytical model for $N = 6$**

1
2 In this section, we develop analytical models based on idealization of the two
3 deformation modes identified in the previous section. The idealization will invoke rigid-
4 perfectly plastic material model and travelling and stationary plastic hinge lines in the
5 deformation mechanisms.
6
7
8
9
10
11
12

13 **4.1 Non-rigid deployment mode I**
14
15

16 **4.1.1 Basic deployment element I**
17
18

19 Fig. 8 shows the formation process of the assumed deployment mode, which
20 demonstrated in a series of successively deformed configurations in FEA. For an origami
21 bellows with hexagonal cross-section, it consists of a module with a total initial height of
22 $2h \sin \theta_0$, where θ_0 is initial pre-folding angle, and six basic deployment elements. In the
23 formation of a single development element, facet bending forms around the folding vertexes
24 to satisfy kinetically admissible conditions, and each element eventually fully deploys. As
25 tension progresses, pre-folding angle increases, and a series of such deployment modes occur
26 asynchronously for a long origami bellows. In this deployment mode, one inclined hinge
27 transforms into two travelling subhinges, and they propagate in the opposite directions.
28
29
30
31
32
33
34
35
36
37
38
39
40
41
42



43
44 **Fig. 8.** Sequentially deformed configurations in FEA of origami bellows with hexagonal
45 cross-section which deployed as non-rigid deployment mode I ($\theta_0 = 40^\circ$, $h = 12\text{mm}$, $t =$
46 0.3mm , $a = 38\text{mm}$, and $b = 3\text{mm}$).
47
48
49
50
51
52
53
54
55
56
57
58
59
60
61
62
63
64
65

4.1.2 Idealized deployment mechanism

For those origami bellows deployed as non-rigid deployment mode I, two types of plastic hinge lines generated along creases, horizontal stationary hinges and inclined travelling hinges, are involved. It means that during the deployment of the area between adjacent modules, both bending energy and extension energy contribute to the plastic deformation.

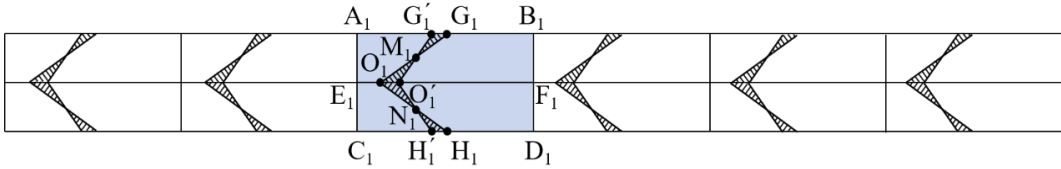
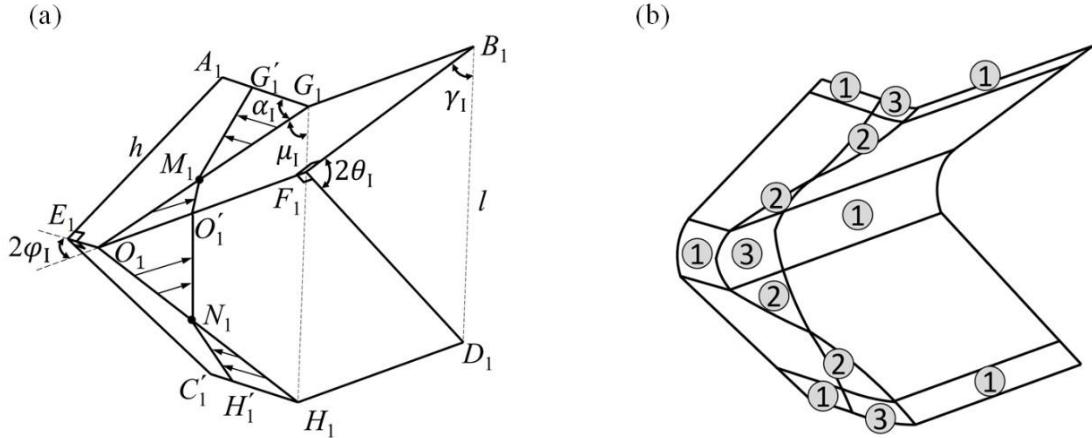


Fig. 9. The flatten view of one hexagonal module deployed as non-rigid deployment mode I.

A schematic diagram of the distribution of plastic hinges lines is shown in Fig. 9. For a basic deployment element I shaded in blue, four inclined travelling plastic hinges are involved during the deformation, i.e., G'_1M_1 , O'_1M_1 , O'_1N_1 and $N_1H'_1$. As indicated in the previous study [54], for the travelling areas, the materials were first bent to a radius r and then backed to be flattened. For the basic element herein, the radius r of four travelling areas is assumed to be constant during deployment, points M_1 and N_1 are assumed to be the middle point of line O_1G_1 and O_1H_1 , respectively. It should be noted that the position of the point M_1 and N_1 will be changed for other possible deformation modes. Furthermore, in-plane deformation occurs in the localized region around the intersecting points of two inclined hinge lines, forming a toroidal surface. Besides, all the horizontal lines, such as $A_1G'_1$, G_1B_1 , E_1O_1 , O'_1F_1 , $C_1H'_1$ and H_1D_1 , are stationary hinge lines. Noting that the length of all the stationary hinges decreases within a small range during the deformation process. In this study, we assume that the length of stationary hinges is set as the average of their original and final lengths. In Fig. 9, travelling plastic deformation takes place only in the shadows, and the

1 inclined lines travel through the corresponding shadow areas. Eventually, the plates bounded
 2 by horizontal hinges rotate around the hinges to achieve a structural deployment. In this basic
 3 deployment element, the entire surface of the structure is continuous, which means that both
 4 bending and in-plane deformation occur to ensure a continuous deployment process.
 5
 6
 7
 8
 9



31 **Fig. 10.** Geometry (a) and deformation areas (b) of basic deployment element as non-rigid
 32 deployment mode I. Letters in (a) corresponds to those in Fig 9. The arrows indicate the
 33 direction of travelling hinges and the area swept. Numbers in (b) indicate three different
 34 kinds of deformation zones.
 35
 36
 37
 38
 39

40
 41
 42
 43 Fig. 10 shows the geometry of an idealized basic deployment element I. Travelling
 44 hinges originate from the inclined lines at one corner, O_1G_1 and O_1H_1 . As the basic element
 45 deploys, the travelling area increases, and each inclined line transforms into two sublines
 46 sweeping in the opposite directions, as indicated by the arrows, generating four travelling
 47 plastic hinges. In an ideal model, the pre-folding angle between the adjacent plates bonded by
 48 the horizontal hinge O_1F_1 is $2\theta_I$, and the initial value of the pre-folding angle is $2\theta_{I0}$. The
 49 inclined angle between the horizontal line and travelling hinge is α_I , and the corresponding
 50

initial value is α_{I0} . Theoretically, θ_I and α_I will increase progressively from their initial value
 1 to 90° , respectively. However, the creases are extremely difficult to completely flatten due to
 2 the initially sharp folding line. Additionally, the predicted mean tensile force should be
 3 calculated considering the effective displacement in Eq. (7). Therefore, the predicted tensile
 4 force-displacement curve should firstly be obtained. Another significant parameter is the
 5 rotational angle between two adjacent elements along the circumference, $2\varphi_I$. For an origami
 6 bellows with six basic elements in a module, $\varphi_I = 60^\circ$.
 7
 8
 9
 10
 11
 12
 13
 14
 15
 16
 17

Other two important angles are examined. One is the angle between the inclined line
 18 $O_I G_I$ and the tube axis, μ_I ; the other is the angle between the side of the plate and the tube
 19 axis, γ_I . They satisfy the following geometrical relationships.
 20
 21
 22
 23
 24
 25
 26
 27

$$\tan \mu_I = \frac{\tan \gamma_I}{\sin \varphi_I} \quad (9)$$

$$\gamma_I = \frac{\pi - 2\theta_I}{2} \quad (10)$$

$$\tan \alpha_I = \frac{\tan \varphi_{I0}}{\cos \theta_I} \quad (11)$$

4.1.3 Theoretical mean force

In light of the above mentioned, the energy absorbed by the origami bellows can be
 45 divided into three parts: (1) the horizontal stationary plastic hinges; (2) the inclined traveling
 46 plastic hinges; and (3) the toroidal surfaces, as shown in Fig. 10(b).
 47
 48
 49
 50
 51

Energy dissipation in stationary plastic hinges can be calculated as follows:
 52
 53
 54
 55
 56

$$E_{I-1} = M_P \sum L_i \cdot \Delta\theta_i \quad (12)$$

in which L_i and $\Delta\theta_i$ are the length of the stationary hinge lines and the change of the angle between two facets surrounded the folded line i , respectively, M_p is the fully plastic bending moment per unit length.

$$M_p = \frac{1}{4} \sigma_Y t^2 \quad (13)$$

where σ_Y is the material yield stress.

The stationary plastic hinges are the horizontal pre-folding creases of the basic deployment element I marked as area 1 in Fig. 10(b). The pre-folding creases can be categorized into two groups according to their identical change of the angle: pre-folding creases A_1B_1 and C_1D_1 as group I, pre-folding creases E_1F_1 as group II. The total lengths of the pre-folding creases in the two groups can be obtained as L_{I-1} and L_{I-2} , respectively, which can be calculated by

$$L_{I-1} = 2(a + b) \quad (14)$$

$$L_{I-2} = a + b \quad (15)$$

The changes in the angle of the pre-folding creases in groups I and II are $\theta_I - \theta_{I0}$, and $2(\theta_I - \theta_{I0})$, respectively. Therefore, the energy absorbed by the horizontal stationary plastic hinges in one basic deployment element is

$$E_{I-1} = M_p(\theta_I - \theta_{I0})(L_{I-1} + 2L_{I-2}) \quad (16)$$

1 There are four travelling plastic hinges, which have identical length and sweeping area.
 2

3 Taking one pair of travelling hinge lines, O'_1M_1 and O'_1N_1 , as an instance, the energy absorbed
 4 by this part is [29]
 5

$$10 E_{O'_1M_1,O'_1N_1} = \frac{M_P I_{I-1} h^2}{r_I} \quad (17)$$

11 where r_I is the radii of torsion surfaces, which is assumed to be the same for each sweeping
 12 area. I_{I-1} is given below in Eq. (22).
 13

14 Then, the energy absorbed by two pairs of travelling plastic hinge lines is
 15

$$26 E_{I-2} = \frac{2M_P I_{I-1} h^2}{r_I} \quad (18)$$

27 In addition, the stretching energy is dissipated by the torsion surface which exists around
 28 the intersection points, O_1 , G_1 and H_1 , can be calculated as follows.
 29

30 The energy dissipated by the torsion surface around the intersection point O_1 is
 31

$$42 E_{O_1} = \frac{8M_P h r_I I_{I-2}}{t} \quad (19)$$

43 In one basic deployment element I, the energy dissipated around the intersection point G_1
 44 and H_1 is equal, which is half of that of E_{O_1} . The expression of energy absorbed around point
 45
 46
 47
 48 G_1 and H_1 is
 49

$$58 E_{G_1} = E_{H_1} = \frac{4M_P h r_I I_{I-2}}{t} \quad (20)$$

1
2 Then, the total energy absorbed by the torsion surface is
3
4
5
6

$$E_{I-3} = E_{O_1} + E_{G_1} + E_{H_1} = \frac{16M_P h r_I I_{I-2}}{t} \quad (21)$$

10
11
12
13 where I_{I-1} and I_{I-2} are given by
14
15
16
17

$$I_{I-1} = \frac{\sqrt{3}}{3} \int_{\frac{\pi-2\theta_{I0}}{2}}^{\frac{\pi-2\theta_I}{2}} \frac{\cos \gamma_I}{\sin \alpha_I} d\gamma_I \quad (22)$$

$$I_{I-2} = \sqrt{3} \int_{\frac{\pi-2\theta_{I0}}{2}}^{\frac{\pi-2\theta_I}{2}} \cos \gamma_I \left\{ \frac{\sqrt{3}}{2} \sin \left(\frac{1}{3} \mu_I \right) + \frac{1}{2} \left[1 - \cos \left(\frac{1}{3} \mu_I \right) \right] \right\} d\gamma_I \quad (23)$$

23
24 There are N basic elements in an N -sided module. For an origami bellows with M
25 modules and free top and bottom ends, the energy absorption dissipation in basic deployment
26 element I is
27
28
29
30

$$E_I = N M E_{I-1} + 0.5N(2M-1)(E_{I-2} + E_{I-3}) \quad (24)$$

31
32
33
34
35
36 The initial height of one module is $2h \sin \theta_{I0}$, and the height of the developed module is
37
38
39
40
41
42
43
44
45 $2h \sin \theta_I$. Applying energy balance between the external tensile work and internal energy
46
47
48 dissipation, we have
49
50
51

$$E_I = P_m^I \cdot 2Mh(\sin \theta_I - \sin \theta_{I0}) \quad (25)$$

in which P_m^I is the theoretical mean tensile force for the origami bellows with hexagonal cross-section which deploys as non-rigid deployment mode I.

Substituting Eqs. (9)-(24) into Eq. (25), all the parameters involved can be obtained except for r_I , which can be determined from the assumption that its value is such that the average force would be a minimum, i.e.,

$$\frac{\partial P_m^I}{\partial r_I} = 0 \quad (26)$$

which yields

$$r_I = \sqrt{\frac{thI_{I-1}}{8I_{I-2}}} \quad (27)$$

The mean tensile force of an origami bellows with hexagonal cross-section with non-rigid mode I is finally derived as

$$P_m^I = \frac{NM_p(\theta_I - \theta_{I0})(L_{I-1} + 2L_{I-2})}{2h(\sin \theta_I - \sin \theta_{I0})} + \frac{NM_p(2M-1)\left(\frac{I_{I-1}h}{r_I} + \frac{8r_I I_{I-2}}{t}\right)}{2M(\sin \theta_I - \sin \theta_{I0})} \quad (28)$$

4.2 Non-rigid deployment mode II

4.2.1 Basic deployment element II

The deformation process of the assumed basic deployment element II is demonstrated in a series of progressively deformed configurations in FEA, as depicted in Fig. 11. In this case,

the hexagonal origami bellows is made up of a module with an initial height of $2h \sin \theta_{II0}$,
 where θ_{II0} is the initial value of pre-folding angle in the mode II, and six basic deployment
 elements. Similar to the basic development element in the non-rigid deployment mode I,
 facets bend around the folding vertexes to satisfy kinetically admissible conditions, and each
 element eventually fully deploys under the axial tension. As tensile progresses, pre-folding
 angle increases and a succession of these deployment modes take place concurrently in a long
 origami bellows. In this deployment mode, one pair of inclined hinges transforms into one
 pair of travelling plastic hinge lines.

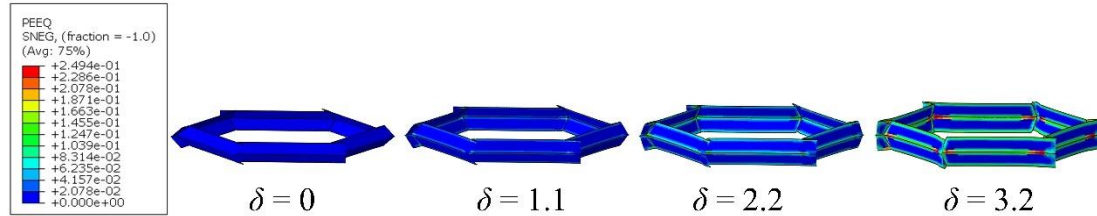


Fig. 11. Sequentially deformed configurations in FEA of origami bellows with non-rigid deployment mode II ($\theta = 40^\circ$, $h = 5\text{mm}$, $t = 0.3\text{mm}$, $a = 38\text{mm}$, and $b = 3\text{mm}$).

4.2.2 Idealized deployment mechanism

For the origami bellows which deployed as non-rigid deployment mode II, modules deploy simultaneously. The geometry of basic deployment element II is presented in Fig. 12. The horizontal lines and inclined lines represent the stationary and travelling plastic hinges, respectively. The shadow regions refer to the sweeping area of the travelling hinges. Here one pair of travelling hinge lines, O'_2G_2 and O'_2H_2 , form. This may be visualized as the hinge lines moving about points G_2 and H_2 , which are fixed, while in the previous deployment mechanism in basic element I, the travelling hinges are moving about points M_1 and N_1 ,

which are assumed to be at the mid-points. As the deformation proceeds, point O_2 moves to O'_2 (Fig. 13(a)). According to the superfolding element theory [55], the basic tensile element in this model consists of horizontal stationary plastic hinges (area 1), a toroidal surface (area 4), and one pair of inclined traveling plastic hinges (area 5), as shown in Fig. 13(b).

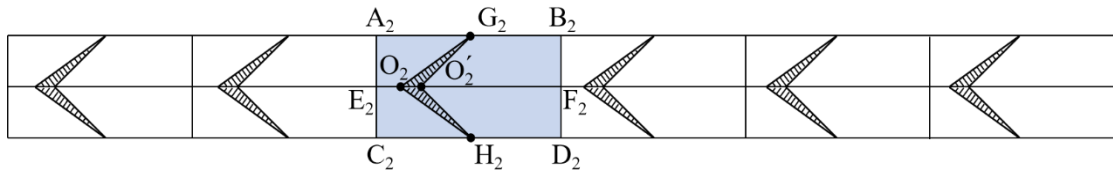


Fig. 12. The flattened view of one hexagonal module with non-rigid deployment mode II.

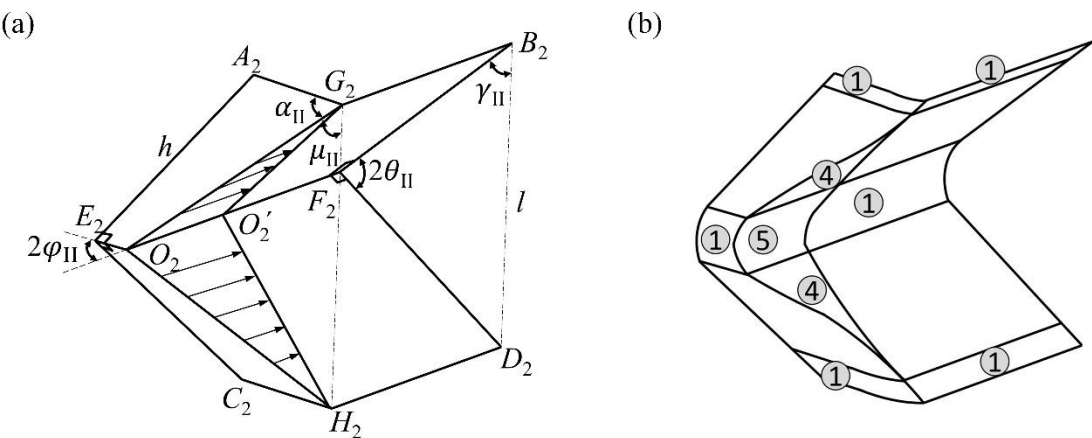


Fig. 13. Geometry (a) and deformation areas (b) of tensile process of basic deployment element with non-rigid deployment mode II.

4.2.3 Analytical mean tensile force

The method of calculating energy absorption is the same as in the previous mode. The energy dissipated in area 1 can be derived from two groups. The total length in each group is $L_{II-1}(A_2B_2 \text{ and } C_2D_2)$ and $L_{II-2}(E_2F_2)$, respectively, and correspondingly pre-folding angles

1
2
3
4
5
6
7
8
9
10
11
12
13
14
15
16
17
18
19
20
21
22
23
24
25
26
27
28
29
30
31
32
33
34
35
36
37
38
39
40
41
42
43
44
45
46
47
48
49
50
51
52
53
54
55
56
57
58
59
60
61
62
63
64
65

are $(\theta_{II} - \theta_{II0})$ and $2(\theta_{II} - \theta_{II0})$, respectively. Thus, the energy dissipated by area1 in basic deployment element II can be calculated as

$$E_{II-1} = M_p(\theta_{II} - \theta_{II0})(L_{II-1} + 2L_{II-2}) \quad (29)$$

in which

$$L_{II-1} = 2(a + b) \quad (30)$$

$$L_{II-2} = a + b \quad (31)$$

The energy dissipated by traveling plastic hinge lines, E_{II-4} , and by the toroidal surfaces, E_{II-5} , can be respectively calculated as

$$E_{II-4} = \frac{4M_p h^2 I_{II-1}}{r_{II}} \quad (32)$$

$$E_{II-5} = \frac{16M_p h r_{II} I_{II-2}}{t} \quad (33)$$

in which r_{II} is the radii of the torsion surfaces of the element deformed as non-rigid deployment mode II. I_{II-1} and I_{II-2} can be generated by

$$I_{II-1} = \frac{\sqrt{3}}{3} \int_{\frac{\pi-2\theta_{II0}}{2}}^{\frac{\pi-2\theta_{II}}{2}} \frac{\cos \gamma_{II}}{\sin \alpha_{II}} d\gamma_{II} \quad (34)$$

$$I_{II-2} = \sqrt{3} \int_{\frac{\pi-2\theta_{II0}}{2}}^{\frac{\pi-2\theta_{II}}{2}} \cos \gamma_{II} \left\{ \frac{\sqrt{3}}{2} \sin \left(\frac{1}{3} \mu_{II} \right) + \frac{1}{2} \left[1 - \cos \left(\frac{1}{3} \mu_{II} \right) \right] \right\} d\gamma_{II} \quad (35)$$

in which angles α_{II} , γ_{II} and μ_{II} satisfy the following geometrical relationships

$$\tan \mu_{\text{II}} = \frac{\tan \gamma_{\text{II}}}{\sin \varphi_{\text{II}}} \quad (36)$$

$$\tan \alpha_{\text{II}} = \frac{\tan \varphi_{\text{II}0}}{\cos \theta_{\text{II}}} \quad (37)$$

Similarly, the radius of the toroidal surface, r_{II} can be determined by

$$\frac{\partial P_m^{\text{II}}}{\partial r_{\text{II}}} = 0 \quad (38)$$

where P_m^{II} is the theoretical mean tensile force for the origami bellow with non-rigid deployment mode II.

Substituting Eqs. (29)-(37) into Eq. (38), we have

$$r_{\text{II}} = \sqrt{\frac{thI_{\text{II}-1}}{4I_{\text{II}-2}}} \quad (39)$$

Then, the total energy, E_{II} , absorbed by origami bellows with M modules and N sides deformed as non-rigid deployment mode II can be calculated as

$$E_{\text{II}} = NM(E_{\text{II}-1} + E_{\text{II}-4} + E_{\text{II}-5}) \quad (40)$$

Energy balance between the external tensile force and internal plastic deformation can be expressed as

$$E_{II} = P_m^{II} \cdot 2Mh(\sin \theta_{II} - \sin \theta_{II0}) \quad (41)$$

The mean tensile force, P_m^{II} , can be obtained as

$$P_m^{II} = \frac{NM_p(\theta_{II} - \theta_{II0})(L_{II-1} + 2L_{II-2})}{2h(\sin \theta_{II} - \sin \theta_{II0})} + \frac{2NM_p\left(\frac{hI_{II-1}}{r_{II}} + \frac{4r_{II}I_{II-2}}{t}\right)}{\sin \theta_{II} - \sin \theta_{II0}} \quad (42)$$

5 Comparison and discussion

5.1 Force-displacement curve

The force versus displacement curves of non-rigid deployment mode I was obtained by considering θ_I as a process parameter, i.e. $\Delta\theta_{Ii}$. Equal steps with $\Delta\theta_{Ii}$ of 1° within the interval $[\theta_{0I} - \theta_I]$ were selected to calculate the force corresponds to each tensile displacement $\delta(\Delta\theta_{Ii})$. Then, Eq. (28) can be expressed as

$$\begin{aligned} P_m^I(\delta_{i+1}) &= \frac{E_{I,i+1} - E_{I,i}}{\Delta\delta_{i+1}} = \\ &= \frac{NM_p(\theta_{I,i+1} - \theta_{I,i})(L_{I-1}(\theta_{I,i}) + 2L_{I-2}(\theta_{I,i}))}{2h(\sin \theta_{I,i+1} - \sin \theta_{I,i})} + \\ &\quad \frac{NM_p(2M - 1)\left[\left(\frac{I_{I-1}(\theta_{I,i})h}{r_I(\theta_{I,i})} + \frac{8r_I(\theta_{I,i})I_{I-2}(\theta_{I,i})}{t}\right)\right]}{2M(\sin \theta_{I,i+1} - \sin \theta_{I,i})} \end{aligned} \quad (43)$$

The corresponding displacement can be worked out. The curves obtained from Eq. (43) are illustrated in Fig. 14. The analytical curves show a slightly lower force than the numerical curves in the first half of the approximate plateau stage. The theoretical model does not

1 consider the energy dissipated by the plastic deformation at the end of the horizontal
2 mountain lines, leading to an underestimate of the response force. As the tensile displacement
3 increased, the analytical curves show higher values than the numerical ones during the second
4 half of the plateau stage. This discrepancy is attributed to the sequential deployment of
5 modules in FEA, whereas the theoretical analysis assumes a simultaneous deployment of
6 modules, which leads to an overestimate of the predicted outcomes. Overall, the comparison
7 of the force-displacement curves obtained by the analytical and numerical results shows a
8 good agreement in both the overall trend and magnitude.
9
10
11
12
13
14
15
16
17
18
19
20
21
22
23
24
25
26
27
28
29
30
31
32
33
34
35
36
37
38
39
40
41
42
43
44
45
46
47
48
49
50
51
52
53
54
55
56
57
58
59
60
61
62

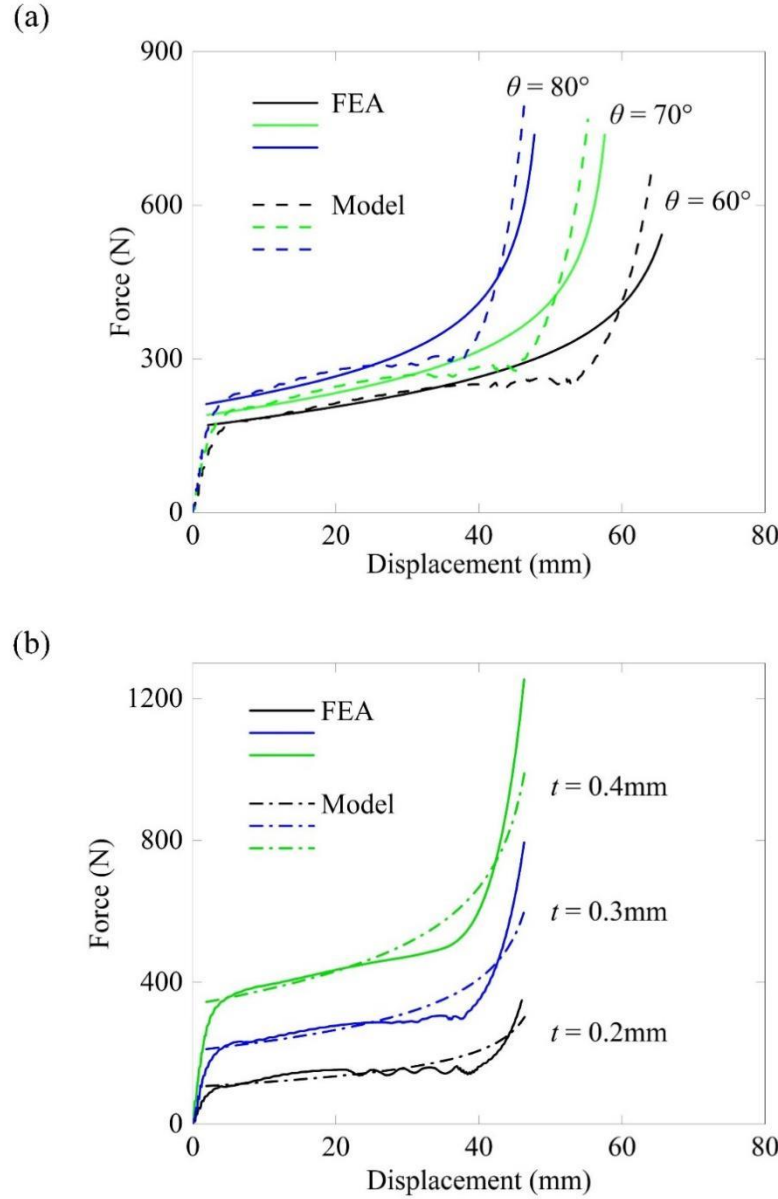


Fig. 14. Force-displacement curves of (a) HEX-60-12-0.3, HEX-70-12-0.3 and HEX-80-12-0.3 with increasing θ , and (b) HEX-80-12-0.2, HEX-80-12-0.3 and HEX-80-12-0.4 with increasing t from FEA and theoretical analysis.

Using the same approach, the analytical force versus displacement curves of non-rigid deployment mode II can be obtained from Eq. (42) as

$$\begin{aligned}
P_m^{\text{II}}(\delta_{i+1}) &= \frac{E_{\text{II},i+1} - E_{\text{II},i}}{\Delta\delta_{i+1}} \\
&= \frac{NM_p(\theta_{\text{II},i+1} - \theta_{\text{II},i})(L_{\text{II}-1}(\theta_{\text{II},i}) + 2L_{\text{I}-2}(\theta_{\text{II},i}))}{2h(\sin\theta_{\text{II},i+1} - \sin\theta_{\text{II},i})} + \\
&\quad \frac{2NM_p\left(\frac{hI_{\text{II}-1}(\theta_{\text{II},i})}{r_{\text{II}}(\theta_{\text{II},i})} + \frac{4r_{\text{II}}(\theta_{\text{II},i})I_{\text{II}-2}(\theta_{\text{II},i})}{t}\right)}{\sin\theta_{\text{II},i+1} - \sin\theta_{\text{II},i}}
\end{aligned} \tag{44}$$

Taking HEX-80-5-0.2 and HEX-80-5-0.3 as examples, the comparison of numerical and predicted results is shown in Fig. 15. The analytical curves are consistently lower than the numerical curves, likely due to the omission of certain plastic deformations that were not accounted for in the models. These include membrane deformations around the end of the mountain horizontal folds and bending of the long horizontal mountain creases. Furthermore, as the wall thickness t increases, the disparity between the numerical and theoretical curves becomes more pronounced. This observation suggests that the deployment mode will shift significantly when t reaches a sufficiently large value.

The accuracy of the analytical models by examining the average tensile force values was also evaluated. The predicted value of mean tensile forces of the bellows with non-rigid deployment modes I and II are presented in Section 5.2.

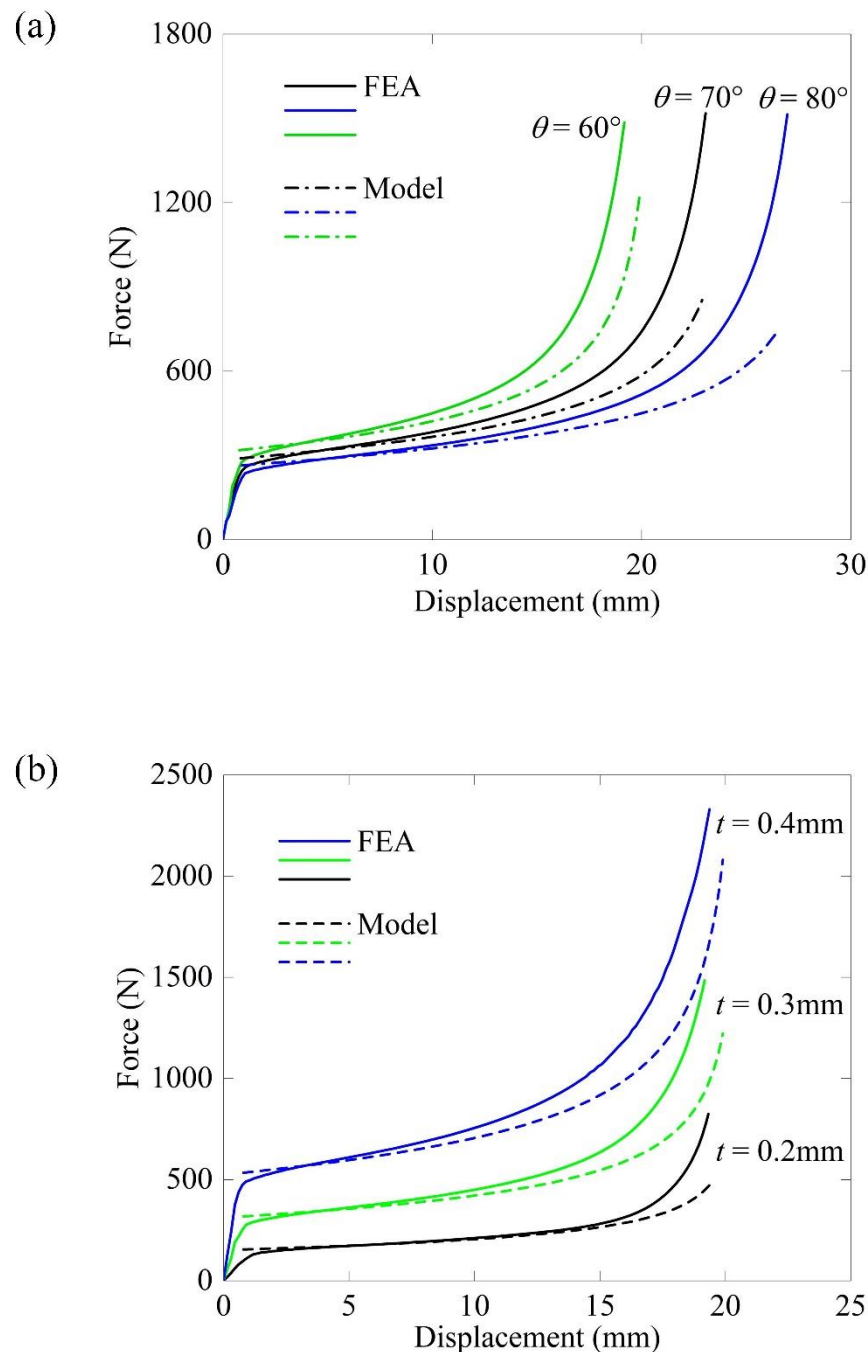


Fig. 15. Force-displacement curves of (a) HEX-60-5-0.3, HEX-70-5-0.3 and HEX-80-5-0.3 with increasing θ and (b) HEX-80-5-0.2, HEX-80-5-0.3 and HEX-80-5-0.4 with increasing t from FEA and theoretical analysis.

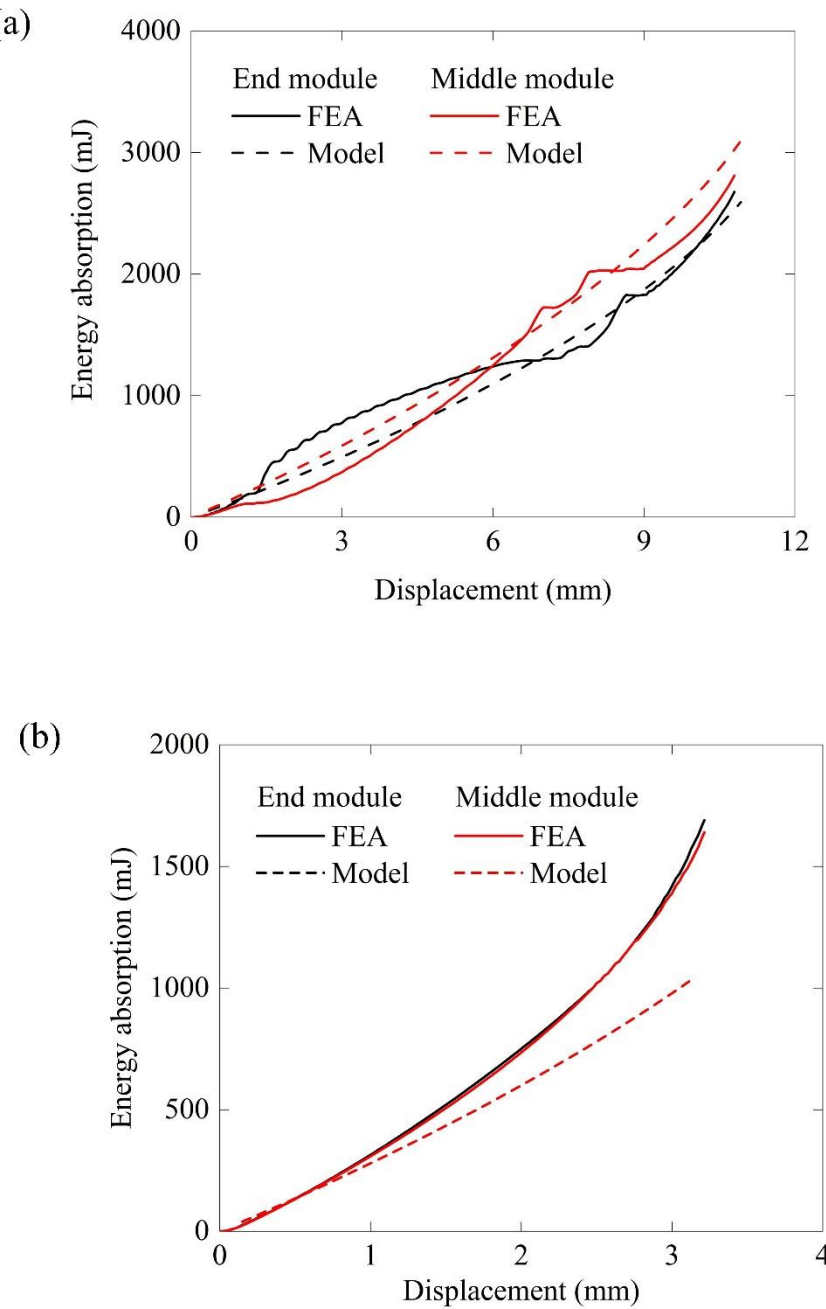


Fig. 16. Comparison of the analytical and numerical energy absorbed by the end module and middle module of (a) HEX-60-12-0.3 deployed in non-rigid mode I and (b) HEX-60-5-0.3 deployed in non-rigid mode II.

To validate the theoretical models further, the theoretical and numerical energy absorbed by the end module and middle module of origami bellows are compared in Fig. 16. The end

modules refer to the boundary modules located at the ends of bellows, while the remaining
1
2
3
4
5
6
7
8
9
10
11
12
13
14
15
16
17
18
19
20
21
22
23
24
25
26
27
28
29
30
31
32
33
34
35
36
37
38
39
40
41
42
43
44
45
46
47
48
49
50
51
52
53
54
55
56
57
58
59
60
61
62
63
64
65

modules are referred to as middle modules. From Fig. 16a, it can be observed that the theoretical values are higher than numerical values for the end module in the range of approximately 1.35mm-6.85mm, but lower for the middle module. This discrepancy arises because in the numerical analysis, the end module deploys first, whereas in the theoretical analysis, all modules are assumed to deploy simultaneously. Consequently, more energy is dissipated through traveling plastic hinges and the toroidal surface in the simulation compared to the theoretical model. However, in the numerical analysis, the middle modules deployed sequentially, whereas in the theoretical model, they were assumed to deploy simultaneously. As a result, the energy absorbed by the theoretical model is expected to be higher than that absorbed by the FE model. From Fig. 16b, it is evident that the theoretical values are lower than the numerical ones due to the omission of certain plastic deformations, such as crease bending and facet bending. Despite these discrepancies, the overall comparison results demonstrate a good agreement, indicating the acceptability of the theoretical analysis for the two deployment modes.

5.2 Mean tensile force

The total energy absorption of the origami bellows with hexagonal cross-section can be obtained by integrating the predicted force over the tensile displacement within the range from 0 to δ_e . The energy efficiency f of the whole progressive tensile process is calculated according to Eq. (8). The predicted mean tensile forces, P_m^I , of the origami bellows deployed as non-rigid mode I are summarized in Table 2. The differences between the analytical and numerical values are less than 7%, demonstrating that the above approach provides an accurate prediction of the mean tensile force for non-rigid deployment mode I.

1
2
3
4
5
6
7
8
9
10
11
12
13
14
15
16
17
18
19
20
21
22
23
24
25
26
27
28
29
30
31
32
33
34
35
36
37
38
39
40
41
42
43
44
45
46
47
48
49
50
51
52
53
54
55
56
57
58
59
60
61
62
63
64
65

Table 2. Comparison of the numerical results and analytical results for the mean tensile force of the origami bellows deformed as non-rigid deployment mode I.

Model	P_m (N)	P_m^I (N)	δ_e (mm)	Difference (%)	
				$ P_m^I - P_m /P_m$	
HEX-60-12-0.3	217.47	231.13	56.34	6.23	
HEX-70-12-0.3	238.28	248.67	47.91	4.36	
HEX-80-12-0.2	135.62	136.29	39.96	0.50	
HEX-80-12-0.3	257.80	268.02	39.96	3.97	
HEX-80-12-0.4	413.09	435.54	39.96	5.43	

Table 3

Comparison of the numerical results and analytical results for the mean tensile force of the origami bellows for the non-rigid deployment mode II.

Model	P_m (N)	P_m^{II} (N)	δ_e (mm)	Difference (%)	
				$ P_m^{II} - P_m /P_m$	
HEX-60-5-0.3	349.58	343.77	23.03	1.66	
HEX-70-5-0.3	377.62	368.61	19.55	2.38	
HEX-80-5-0.3	409.85	396.83	16.27	3.18	
HEX-80-5-0.2	191.43	195.71	16.65	2.24	

The same approach was used to predict the mean tensile force of the origami bellows with hexagonal cross-section deployed as non-rigid deployment mode II. The theoretical results of the mean tensile force of HEX-60-5-0.3, HEX-70-5-0.3, HEX-80-5-0.3, and HEX-80-5-0.2 are listed in Table 3. The difference increases with the pre-folding angle θ and wall thickness t . However, theoretical predictions of the mean tensile force for origami bellows deployed as non-rigid deployment mode II showed reasonable agreement with corresponding numerical results, with a difference of less than 4%.

To investigate the relationship between the mean force and the geometric parameters of the origami bellows deployed in different modes, we first rearrange Eq. (28) as follows:

$$2M(\sin \theta_I - \sin \theta_{I0}) \frac{P_m^I}{M_P} = A_1 \frac{r_I}{t} + A_2 \frac{L_{I-1} + L_{I-2}}{h} + A_3 \frac{h}{r_I} \quad (45)$$

where

$$A_1 = 16I_{I-2} \left(NM - \frac{N}{2} \right) \quad (46)$$

$$A_2 = NM(\theta_I - \theta_{I0}) \quad (47)$$

$$A_3 = 2I_{I-1} \left(NM - \frac{N}{2} \right) \quad (48)$$

By assuming the minimization of the average force with respect to h , the expression for h can be obtained.

$$\frac{\partial P_m^I}{\partial h} = 0 \quad (49)$$

which yields

$$h = A_2^{\frac{1}{2}} A_3^{-\frac{1}{2}} (L_{I-1} + L_{I-2})^{\frac{1}{2}} r_I^{\frac{1}{2}} \quad (50)$$

The expression of r_I can be obtained according to the Eq. (26)

$$r_I = A_1^{-\frac{1}{2}} A_3^{\frac{1}{2}} h^{\frac{1}{2}} t^{\frac{1}{2}} \quad (51)$$

Combining Eq. (50) and Eq. (51), we obtain

$$r_I = A_1^{-\frac{2}{3}} A_2^{\frac{1}{3}} A_3^{\frac{1}{3}} (L_{I-1} + L_{I-2})^{\frac{1}{3}} t^{\frac{2}{3}} \quad (52)$$

$$h = A_2^{\frac{1}{2}} A_3^{-\frac{1}{2}} (L_{I-1} + L_{I-2})^{\frac{2}{3}} r_I^{\frac{1}{2}} \quad (53)$$

Substituting Eq. (13), Eq. (52) and Eq. (53) back into Eq. (45), we have

$$P_m^I = \frac{3\sqrt[3]{A_1 A_2 A_3} \sqrt[3]{(L_{I-1} + L_{I-2})}}{8M(\sin \theta_I - \sin \theta_{I0})} \sigma_Y t^{\frac{5}{3}} \quad (54)$$

Similarly, the relationship between the mean force and the geometric parameters of origami bellows deployed in mode II can be obtained

$$P_m^{II} = \frac{3\sqrt[3]{A_4 A_5 A_6} \sqrt[3]{(L_{II-1} + L_{II-2})}}{8M(\sin \theta_{II} - \sin \theta_{II0})} \sigma_Y t^{\frac{5}{3}} \quad (55)$$

where

$$A_4 = 16I_{II-2}NM \quad (46)$$

$$A_5 = NM(\theta_{II} - \theta_{II0}) \quad (47)$$

$$A_6 = 4I_{II-1}NM \quad (48)$$

From the above equation, it can be found that, for typical values of pre-folding angle, cross-section and number of modules of an origami bellows, both P_m^I and P_m^{II} are proportional to $t^{\frac{5}{3}}$. This finding indicates that the empirical model for the mean force, as observed in [51] with a power law relationship of $t^{1.67}$, can be supported and validated from mechanics of the deformation. Additionally, we calculated the predicted value of mean force for the case deployed as mode I by using the basic deployment element I and II, respectively. It can be found that the predicted value obtained from basic deployment element II is always larger

than that obtained from basic deployment element I. This indicated that plastic deformation
obeys the principle of minimum potential energy. In other words, the origami bellows
exhibits a preference for deploying as a low-energy mechanism, specifically mode I.

Overall, the theoretical predictions for the mean tensile force of the origami bellows with
hexagonal cross-section deployed as two deployment modes show reasonable agreement with
the corresponding numerical results. The described analytical models can offer guidance in
designing hexagonal origami bellows by selecting suitable geometric and material parameters
to achieve the desired mean tensile force.

6 Conclusions

In this paper, the quasi-static mechanical behavior and energy absorption of origami
bellows with polygonal cross-section under axial tension have been numerically and
analytically studied. The effects of the polygonal cross-section on the mechanical behavior
and energy absorption of the bellows have been numerically investigated. In addition, two
deployment modes of bellows with hexagonal cross-section have been described in detail,
and the corresponding theoretical models for each mode has been validated against numerical
results. The study leads to the following conclusions:

1. A smooth force-displacement curve with no excessive initial peak force can be
obtained from all polygonal cross-section bellows. The tensile process in origami
bellows involves both crease and facet bending, with significant plastic deformation
starting from the fold vertices and then progressing along the fold lines.
2. The plateau force was found to increase with the increasing number of polygonal
sides N , resulting in an increase of both the mean tensile force P_m and specific
energy absorption SEA by 22.05% and 23.85%, respectively when N increased from

1
2
3
4
5
6
7
8
9
10
11
12
13
14
15
16
17
18
19
20
21
22
23
24
25
26
27
28
29
30
31
32
33
34
35
36
37
38
39
40
5 to 8. The origami bellows with a higher N can be regarded as a better candidate for application as an energy absorption device.

3. The origami bellows with different cross-sections show different deployment modes under axial tensile loading. Two types of non-rigid deployment modes are identified in the hexagonal cross-section bellows, i.e., non-rigid deployment mode I and non-rigid deployment mode II. The progressive deployment around the stationary hinges and traveling hinges is involved in developing the corresponding basic deployment element. The hexagonal cross-section bellows with wall thickness of 0.3mm with non-rigid mode II show a 60% improvement in both SEA and P_m compared with their counterparts with non-rigid mode I.
4. The two types of non-rigid deployment modes present in hexagonal cross-section bellows have been investigated theoretically. The predicted force history and the values of mean tensile force have been validated against numerical results, and the comparison showed a reasonable agreement between the two.

Other deployment modes in the polygonal cross-section bellows may be present and further investigations may be needed to develop their analytical models.

41 CRediT authorship contribution statement

42
43
44 **Xinyi Zhang:** Conceptualization, Data curation, Formal analysis, Methodology,
45 Investigation, Software, Writing - Original draft. **Dora Karagiozova:** Methodology, Formal
46 analysis, Validation, Writing - review & editing. **Guoxing Lu:** Conceptualization,
47 Methodology, Validation, Formal analysis, Writing - review & editing, Supervision. **Yvonne**
48
49 **Durandet:** Supervision, Project administration, Funding acquisition. **Shanghai Wang:**
50 Resources, Supervision, Project administration.
51
52
53
54
55
56
57
58
59
60
61
62
63
64
65

1
2
3
4
5
6
7
8
9
10 **Acknowledgment**

11 This research is financially supported by Australia Department of Industry Innovation
12 and Science under Automotive Engineering Graduate Program (AEGP) (AEGP000019).
13
14

15 **References**
16
17
18
19
20
21
22
23
24
25
26
27
28
29
30
31
32
33
34
35
36
37
38
39
40
41
42
43
44
45
46
47
48
49
50
51
52
53
54
55
56
57
58
59
60
61
62
63
64
65

- [1] Lu G, Yu TX, Energy absorption of structures and materials. Cambridge, UK: Woodhead Publishing Limited; 2003.
- [2] Ma J, Chai S, Chen Y. Geometric design, deformation mode, and energy absorption of patterned thin-walled structures. *Mech Mater* 2022;168:104269.
- [3] Xiang Y, Wang M, Yu T, Yang L. Key performance indicators of tubes and foam-filled tubes used as energy absorbers. *Int J Appl Mech* 2015;7(04):1550060.
- [4] Song J, Chen Y, Lu G. Axial crushing of thin-walled structures with origami patterns. *Thin-Walled Struct* 2012;54:65-71.
- [5] Li Z, Ma W, Hou L, Xu P, Yao S. Crashworthiness analysis of corrugations reinforced multi-cell square tubes. *Thin-Walled Struct* 2020;150:106708.
- [6] Yang H, Lei H, Lu G. Crashworthiness of circular fiber reinforced plastic tubes filled with composite skeletons/aluminum foam under drop-weight impact loading. *Thin-Walled Struct* 2021;160:107380.
- [7] Ha NS, Pham TM, Chen W, Hao H, Lu G. Crashworthiness analysis of bio-inspired fractal tree-like multi-cell circular tubes under axial crushing. *Thin-Walled Struct* 2021;169:108315.
- [8] Ma W, Li ZX, Xie SC. Crashworthiness analysis of thin-walled bio-inspired multi-cell corrugated tubes under quasi-static axial loading. *Eng Struct* 2020;204:110069.
- [9] Ha NS, Lu G. Thin-walled corrugated structures: A review of crashworthiness designs and energy absorption characteristics. *Thin-Walled Struct* 2020;157:106995.

- [10] Ha NS, Lu G, Xiang X. High energy absorption efficiency of thin-walled conical corrugation tubes mimicking coconut tree configuration. *Int J Mech Sci* 2018;148:409-421.
- [11] Taştan A, Acar E, Güler MA, Kılınçkaya ÜJT-WS. Optimum crashworthiness design of tapered thin-walled tubes with lateral circular cutouts. *Thin-Walled Struct* 2016;107:543-553.
- [12] Magliaro J, Altenhof W, Alpas AT. A review of advanced materials, structures and deformation modes for adaptive energy dissipation and structural crashworthiness. *Thin-Walled Struct* 2022;180:109808.
- [13] Li Y, Fan Z, Hu S, Zhang F, Hu L, Xue Z. Dynamic enhancement mechanism of energy absorption of multi-cell thin-walled tube. *Thin-Walled Struct* 2022;178:109449.
- [14] Jin M, Hou X, Yin G, Yao R, Gao J, Deng Z. Improving the crashworthiness of bio-inspired multi-cell thin-walled tubes under axial loading: Experimental, numerical, and theoretical studies. *Thin-Walled Struct* 2022;177:109415.
- [15] Ming S, Song Z, Zhou C, Du K, Teng C, Wang Y, Xu S, Wang B. The crashworthiness design of metal/CFRP hybrid tubes based on origami-ending approach: Experimental research. *Compos Struct* 2022;279:114843.
- [16] Song Z, Ming S, Du K, Zhou C, Wang Y, Xu S, Wang B. Energy absorption of metal-composite hybrid tubes with a diamond origami pattern. *Thin-Walled Struct* 2022;180:109824.
- [17] Wang J, Liu Y, Wang K, Yao S, Peng Y, Rao Y, Ahzi S. Progressive collapse behaviors and mechanisms of 3D printed thin-walled composite structures under multi-conditional loading. *Thin-Walled Struct* 2022;171:108810.
- [18] Rossi A, Fawaz Z, Behdinan K. Numerical simulation of the axial collapse of thin-walled polygonal section tubes. *Thin-Walled Struct* 2005;43(10):1646-1661.

- [19] Alavi Nia A, Haddad Hamedani J. Comparative analysis of energy absorption and deformations of thin walled tubes with various section geometries. *Thin-walled struct* 2010;48(12):946-954.
- [20] Yamashita M, Tange Y, Nishimura N, Hattori T. Quasi-Static and Dynamic Axial Crushing of Various Polygonal Tubes. *Key Eng. Mater* 2007;340-341:1399-1404.
- [21] Liu W, Lin Z, Wang N, Deng X. Dynamic performances of thin-walled tubes with star-shaped cross section under axial impact. *Thin-Walled Struct* 2016;100:25-37.
- [22] Fu J, Liu Q, Liufu K, Deng Y, Fang J, Li Q. Design of bionic-bamboo thin-walled structures for energy absorption. *Thin-Walled Struct* 2019;135:400-413.
- [23] Sun F, Lai C, Fan H, Fang D. Crushing mechanism of hierarchical lattice structure. *Mech. Mater* 2016;97:164-183.
- [24] Li W, Luo Y, Li M, Sun F, Fan H. A more weight-efficient hierarchical hexagonal multi-cell tubular absorber. *Int J Mech Sci* 2018;140:241-249.
- [25] Alexander JM. An approximate analysis of the collapse of thin cylindrical shells under axial loading. *Q J Mech Appl Math* 1960;13(1):10-15.
- [26] Abramowicz W, Jones N. Dynamic axial crushing of circular tubes. *Int J Impact Eng* 1984;2(3):263-281.
- [27] Wierzbicki T, Bhat SU, Abramowicz W, Brodkin D. Alexander revisited—A two folding elements model of progressive crushing of tubes. *Int J Solids Struct* 1992;29(24):3269-3288.
- [28] Lu G, Yu JL, Zhang JJ, Yu TX. Alexander revisited: upper- and lower-bound approaches for axial crushing of a circular tube. *Int J Mech Sci* 2021;206:106610.
- [29] Wierzbicki T, Abramowicz W. On the crushing mechanics of thin-walled structures. *J. Appl. Mech.* 1983;50(4a):727-734.

- [30] Abramowicz W. The effective crushing distance in axially compressed thin-walled metal columns. *Int J Impact Eng* 1983;1(3):309-317.
- [31] Shen Z, Zhao Y, Zhong H, Tang K, Chen Y, Xiao Y, Yi J, Liu S, and Wang Z. Soft origami optical-sensing actuator for underwater manipulation. *Front. Robot. AI* 2021;7:616128.
- [32] Ma J, Dai H, Shi M, Yuan L, Chen Y, You Z. Quasi-static axial crushing of hexagonal origami crash boxes as energy absorption devices. *Mech. Sci.* 2019;10(1):133-143.
- [33] Fan Z, Lu G, Yu TX, Liu K. Axial crushing of triangular tubes. *Int J Appl Mech* 2013;5(1):1350008.
- [34] Cai J, Deng X, Zhou Y, Feng J, Tu Y. Bistable behavior of the cylindrical origami structure with kresling pattern. *J Mech Des* 2015;137(6):061406.
- [35] Cai J, Deng X, Feng J, Zhou Y. Geometric design and mechanical behavior of a deployable cylinder with Miura origami. *Smart Mater Struct* 2015;24(12).
- [36] Overvelde JTB, De Jong TA, Shevchenko Y, Becerra SA, Whitesides GM, Weaver JC, Hoberman C, Bertoldi K. A three-dimensional actuated origami-inspired transformable metamaterial with multiple degrees of freedom. *Nat. Commun* 2016;7(1):10929.
- [37] Xiang XM, Lu G, You Z. Energy absorption of origami inspired structures and materials. *Thin-Walled Struct* 2020;157:107130.
- [38] Ma J, You Z. Energy absorption of thin-walled square tubes with a prefolded origami pattern—part I: geometry and numerical simulation. *J Appl Mech* 2013;81(1):011003.
- [39] Liu Y, Cai J, Feng J. Buckling suppression of a thin-walled Miura-origami patterned tube. *PLOS ONE* 2022;17(7):e0270228.
- [40] Jensen FV, Concepts for retractable roof structures. University of Cambridge, Cambridge, UK, Ph.D thesis 2004.

- [41] Sharma H, Upadhyay SH. Folding pattern design and deformation behavior of origami based conical structures. *Adv Space Res* 2021;67(7):2058-2076.
- [42] Fonseca LM, Rodrigues GV, Savi MA. An overview of the mechanical description of origami-inspired systems and structures. *Int J Mech Sci* 2022;223:107316.
- [43] Yuan H, Pikul JH, Sung CR. Programmable 3-D surfaces using origami tessellations. Proceedings of the 7th international meeting on origami in science, mathematics and education 2018.
- [44] Yasuda H, Yang J. Reentrant origami-based metamaterials with negative poisson's ratio and bistability. *Phys Rev Lett* 2015;114(18):185502.
- [45] Ishida S, Uchida H, Shimosaka H, Hagiwara I. Design and numerical analysis of vibration isolators with quasi-zero-stiffness characteristics using bistable foldable structures. *J Vib Acoust* 2017;139(3):031015.
- [46] Jeon B-G, Kim S-W, Yun D-W, Ju B-S, Son H-Y. An experimental study on seismic performance evaluation of multi-ply bellows type expansion joint for piping systems. *Sustainability* 2022;14(22):14777.
- [47] Xiang XM, Lu G, Li ZX, Lv Y. Finite element analysis and experimental study on a bellows joint. *Eng. Struct* 2017;151:584-598.
- [48] Xie L, Yang C, Li A, Lu J, Zeng D. Experimental investigation of the seismic performance of flexible pipes for seismically isolated buildings. *Eng. Struct* 2020;222:111132.
- [49] Lee D-O, Park G, Han J-H. Experimental study on on-orbit and launch environment vibration isolation performance of a vibration isolator using bellows and viscous fluid. *Aerosp* 2015;45:1-9.

- [50] Elyasi N, Shahzamanian M, Lin M, Westover L, Li Y, Kainat M, Yoosef-Ghodsi N,
Adeeb S. Prediction of tensile strain capacity for X52 steel pipeline materials using
the extended finite element method. *Appl Mech* 2021;2(2):209-225.
- [51] Zhang X, Wang S, Durandet Y, Palanisamy S, Lu G. Energy absorption behavior of
origami bellows under tension. *Int J Mech Sci* 2023;246:108143.
- [52] Reid A, Lechenault F, Rica S, Adda-Bedia M. Geometry and design of origami bellows
with tunable response. *Physical Review E* 2017;95(1):013002.
- [53] Chen W, Misra S, Gao Y, Lee Y, Koditschek DE, Yang S, Sung CR. A programmably
compliant origami mechanism for dynamically dexterous robots. *IEEE Robot*
2020;5(2):2131-2137.
- [54] Meng Q, Al-Hassani STS, Soden PD. Axial crushing of square tubes. *Int J Mech Sci*
1983;25(9):747-773.
- [55] Wierzbicki T, Abramowicz W. On the crushing mechanics of thin-walled structures. *J
Appl Mech* 1983;50(4a):727-734.

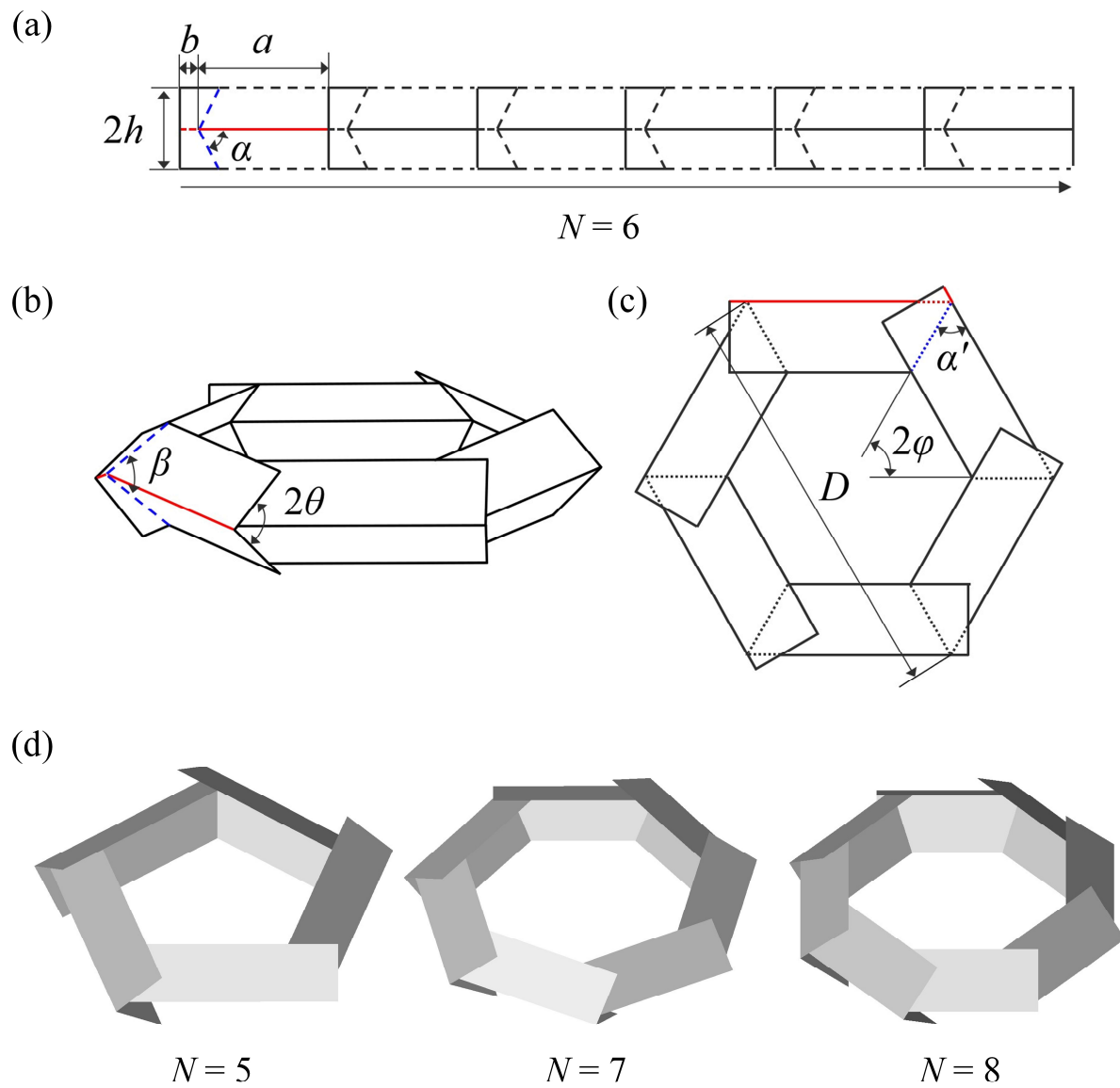


Fig. 1. (a) A flat pleated pattern for one module with hexagonal cross-section. (b) A folded module with hexagonal cross-section. (c) Top view of origami bellows with hexagonal cross-section. (d) A single folded module with pentagonal ($N = 5$), heptagonal ($N = 7$), and octagonal ($N = 8$) cross-section.

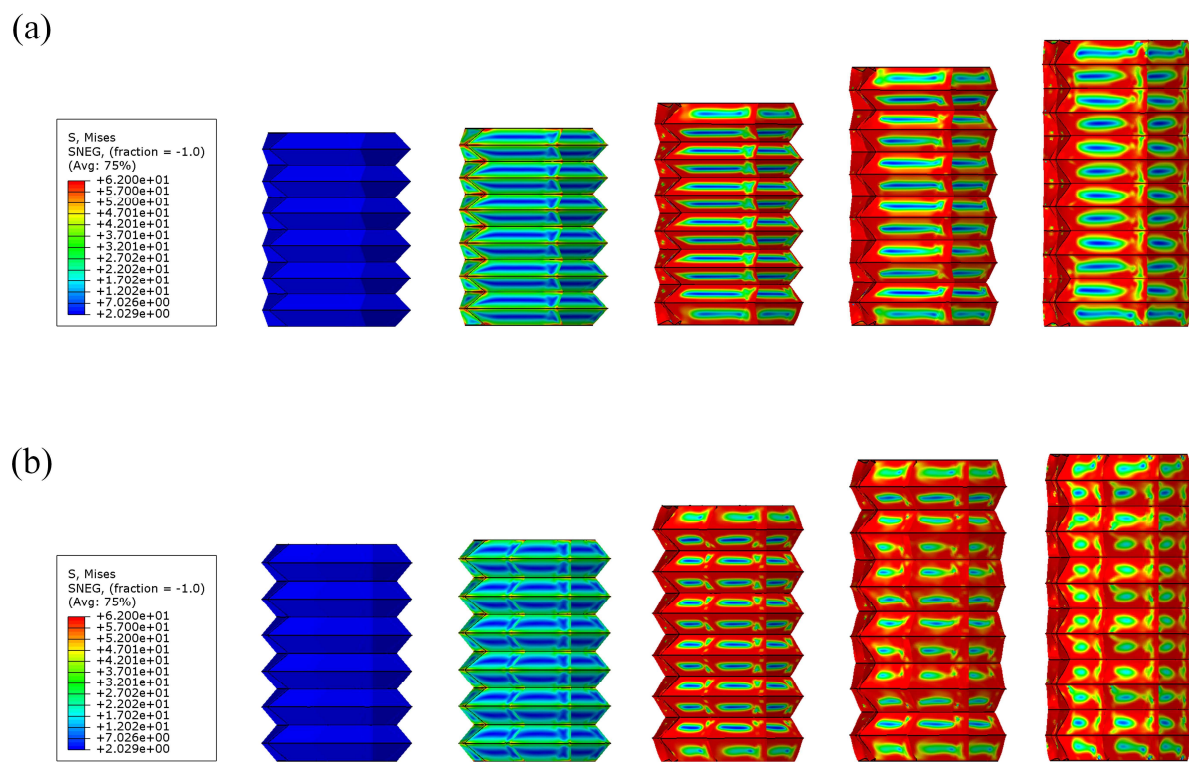


Fig. 2. Tensile deformation process with von Mises stress contours of (a) PEN-80-12-0.3 and (b) OCT-80-12-0.3.

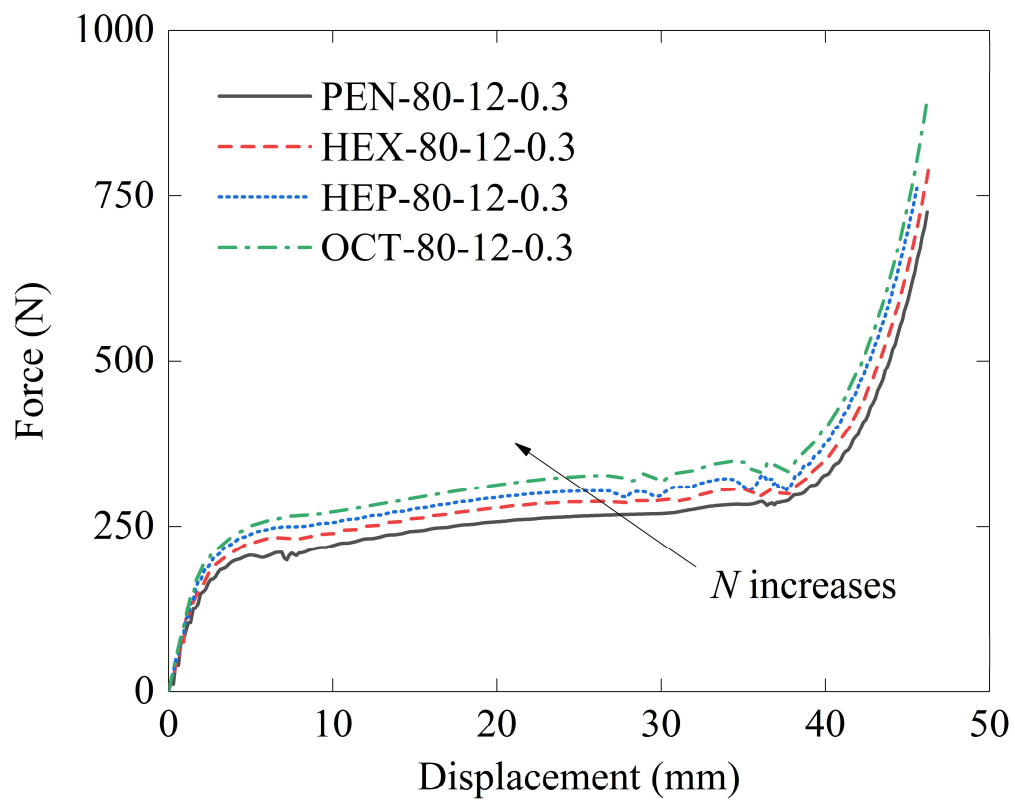
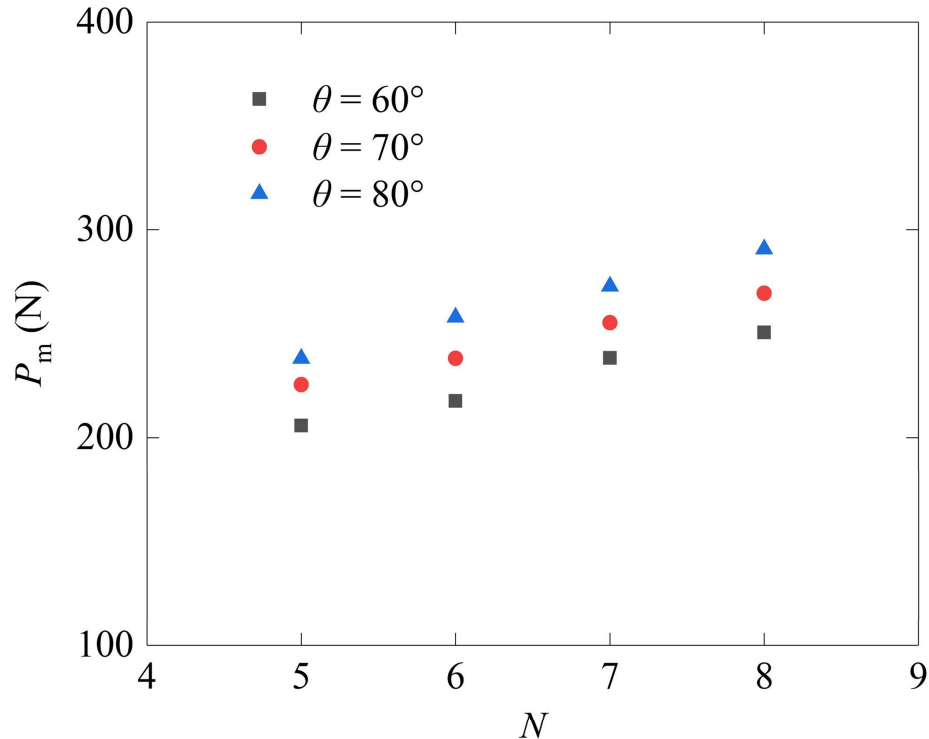


Fig. 3. Force-displacement curves for origami bellows with different polygonal cross-sections ($b = 3\text{mm}$, $h = 12\text{mm}$, $2\theta = 80^\circ$, $M = 6$, $t = 0.3\text{mm}$). N is from 5 to 8.

(a)



(b)

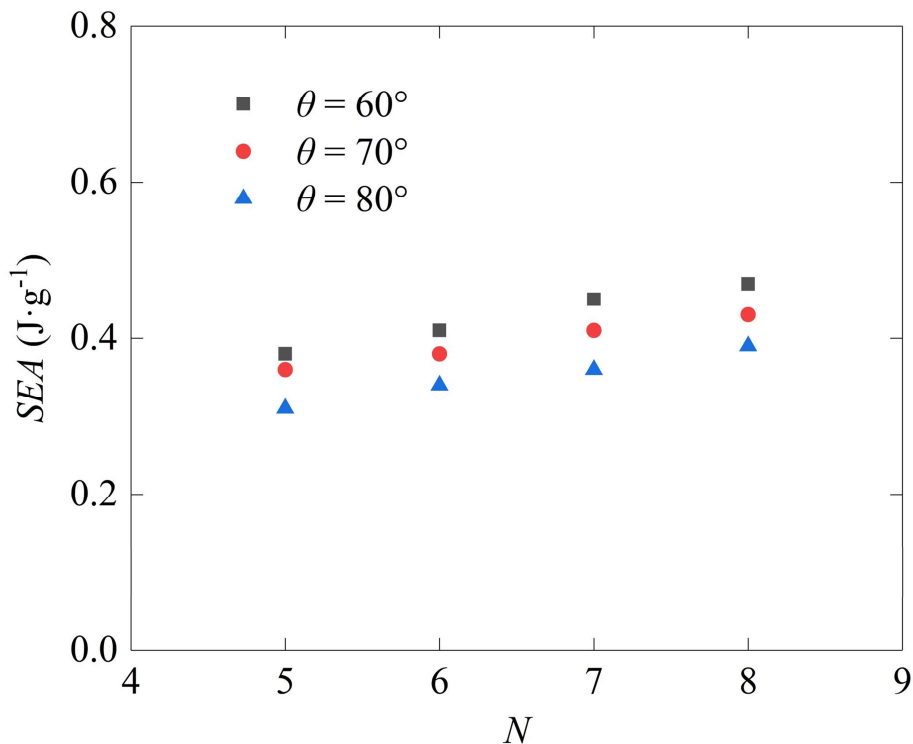


Fig. 4. SEA and P_m of origami bellows with different polygonal cross-sections N and different pre-folding angle 2θ ($h = 12\text{mm}$ and $t = 0.3\text{mm}$).

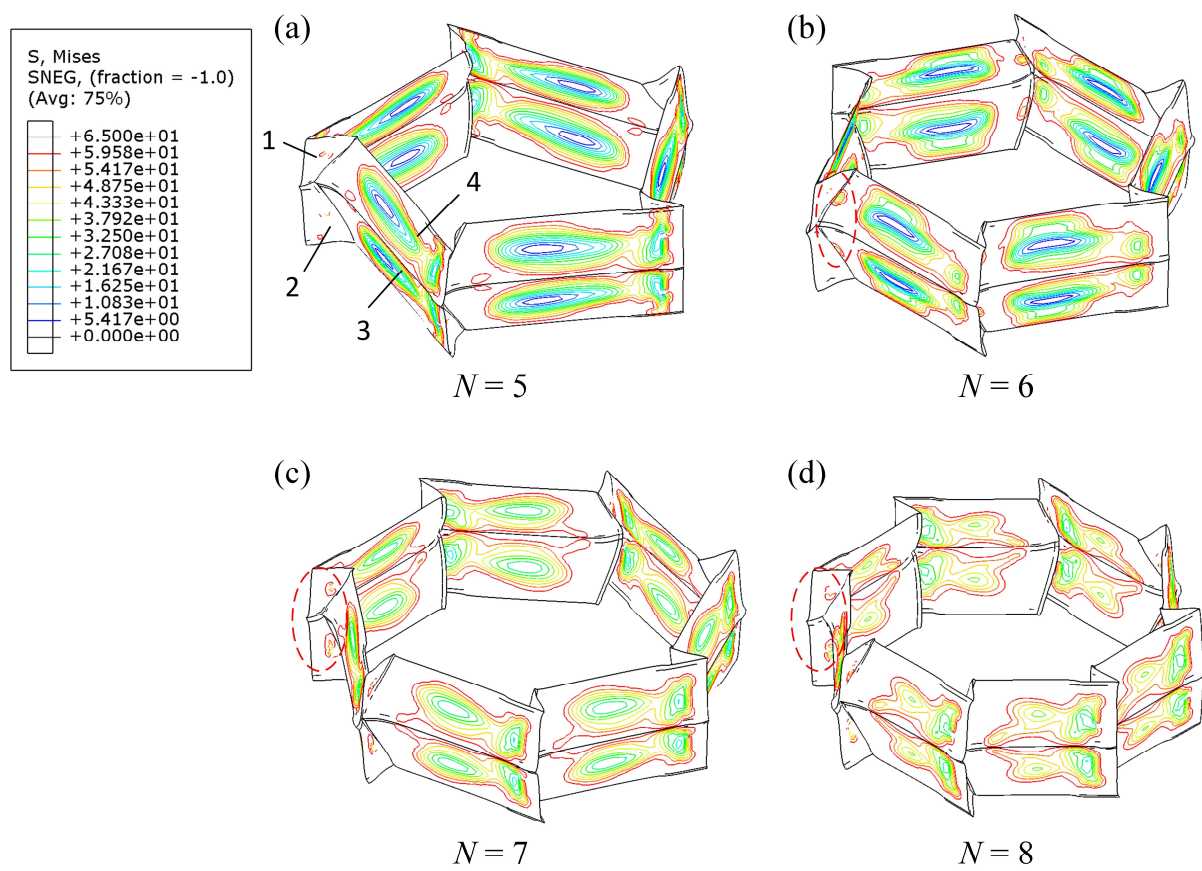


Fig. 5. Mises stress contours of single fully deployed module of (a) PEN-80-12-0.3, (b) HEX-80-12-0.3, (c) HEP-80-12-0.3 and (d) OCT-80-12-0.3.

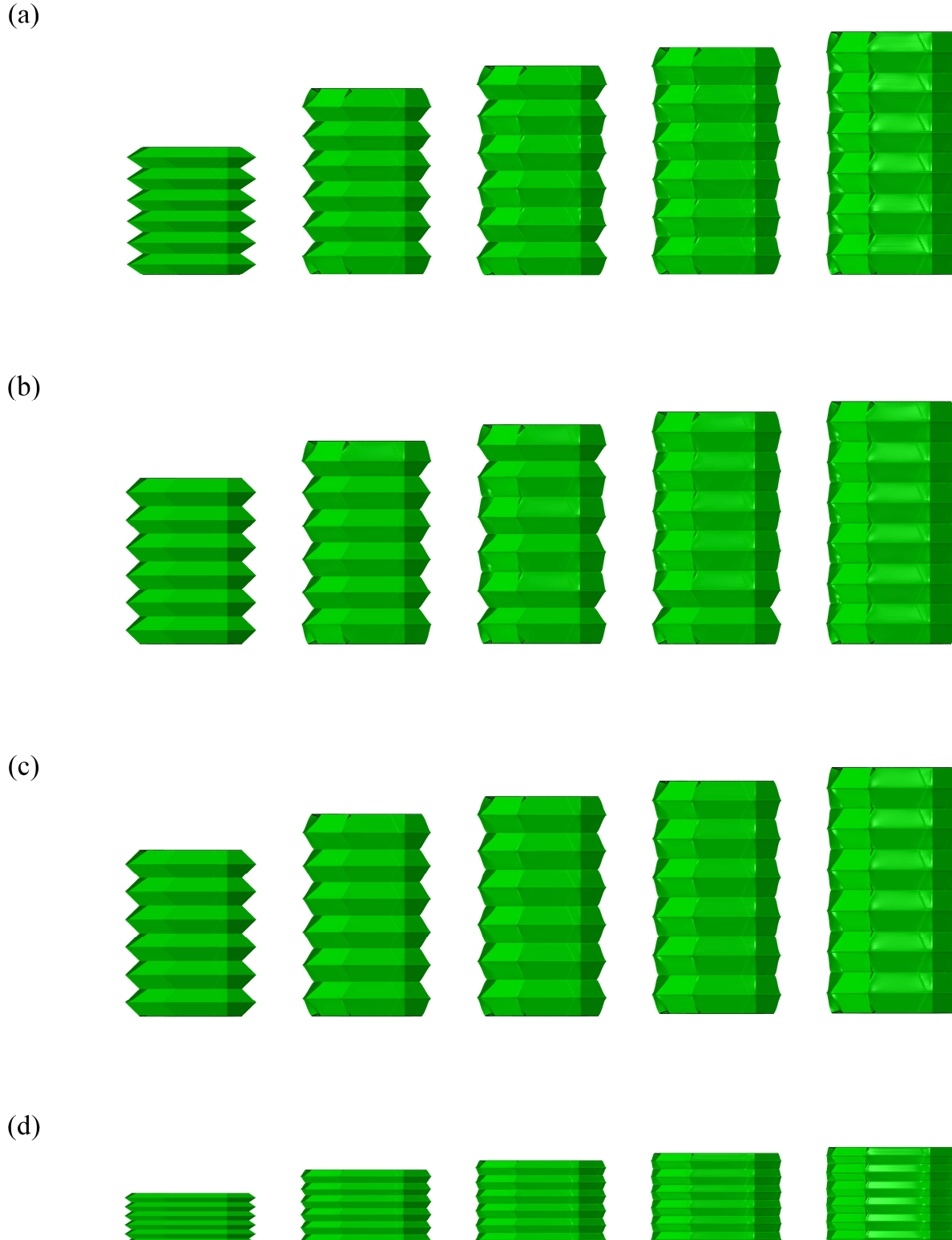


Fig. 6. Tensile deformation process of (a) HEX-60-12-0.3, (b) HEX-80-12-0.2, (c) HEX-80-12-0.4 and (d) HEX-60-5-0.3. The displacements are 64mm, 46mm, 46mm and 26.4mm, respectively.

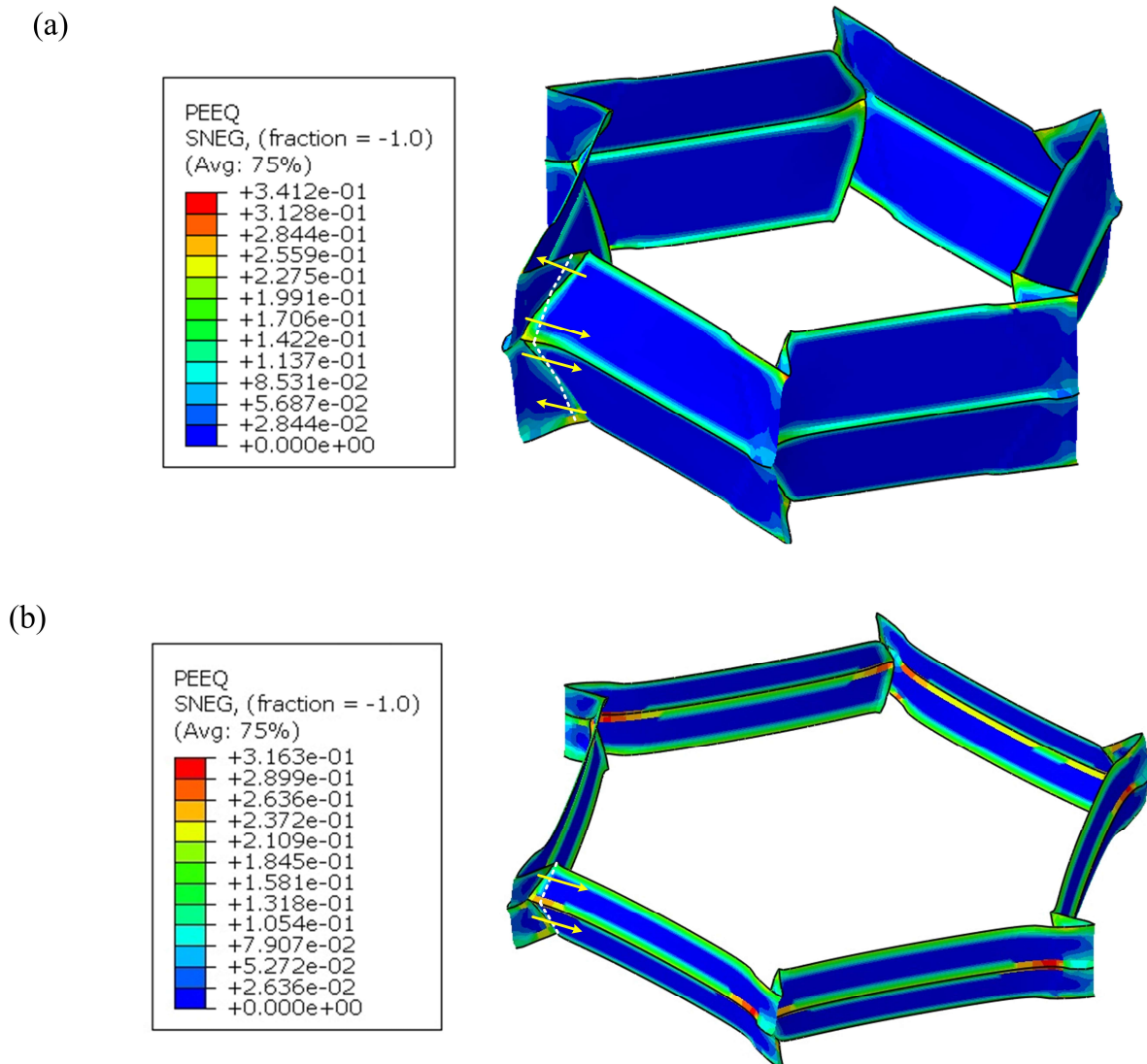


Fig. 7. Equivalent plastic strain contour map of deformed configurations of single module of (a) HEX-60-12-0.3 ($h/t = 40$) and (b) HEX-60-5-0.3 ($h/t = 16.67$).

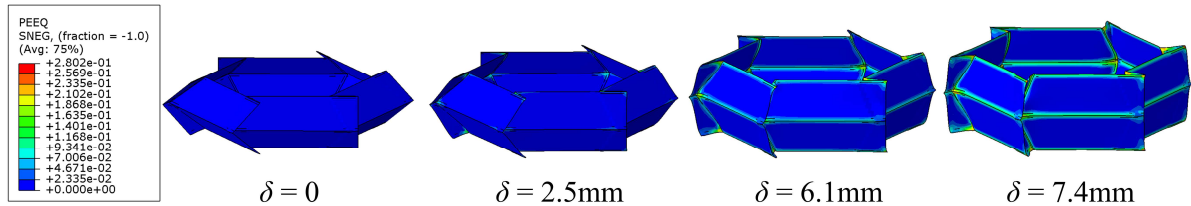


Fig. 8. Sequentially deformed configurations in FEA of origami bellows with hexagonal cross-section which deployed as non-rigid deployment mode I ($\theta_0 = 40^\circ$, $h = 12\text{mm}$, $t = 0.3\text{mm}$, $a = 38\text{mm}$, and $b = 3\text{mm}$).

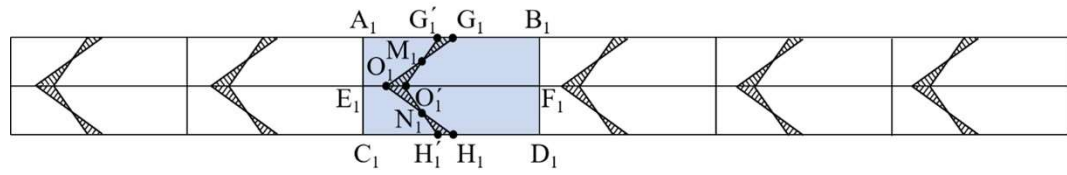


Fig. 9. The flatten view of one hexagonal module deployed as non-rigid deployment mode I.

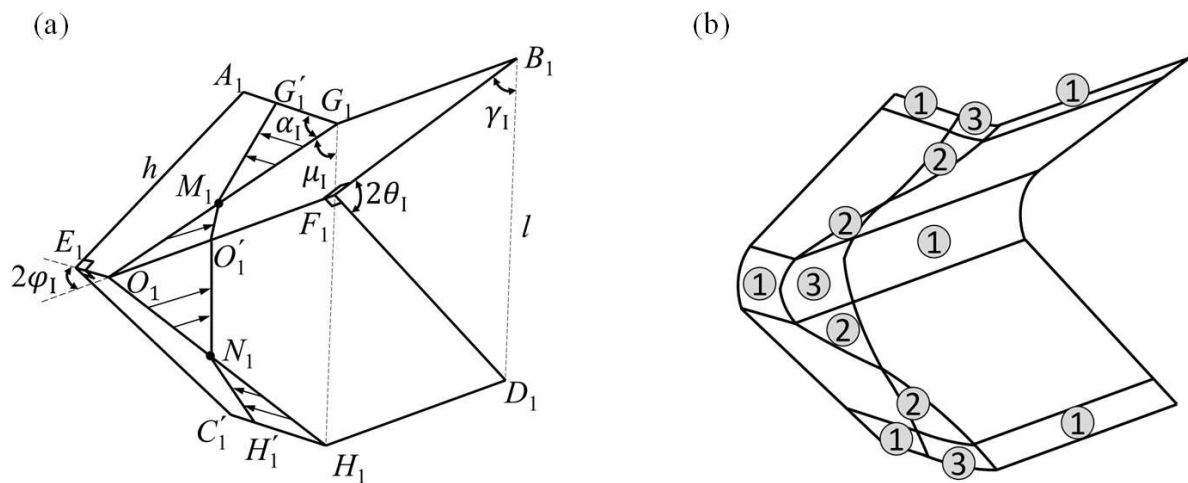


Fig. 10. Geometry (a) and deformation areas (b) of basic deployment element as non-rigid deployment mode I. Letters in (a) corresponds to those in Fig 9. The arrows indicate the direction of travelling hinges and the area swept. Numbers in (b) indicate three different kinds of deformation zones.

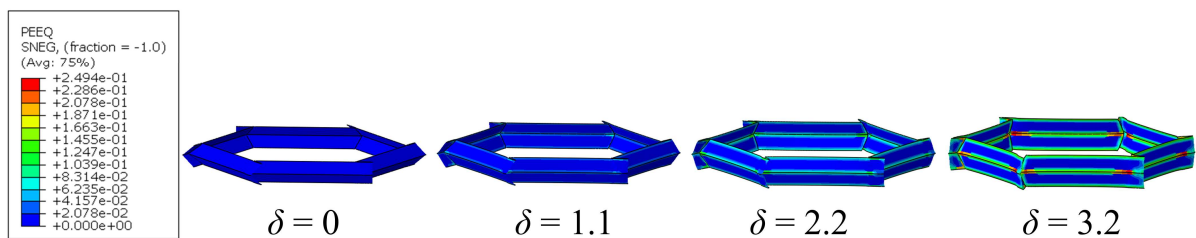


Fig. 11. Sequentially deformed configurations in FEA of origami bellows with non-rigid deployment mode II ($\theta = 40^\circ$, $h = 5\text{mm}$, $t = 0.3\text{mm}$, $a = 38\text{mm}$, and $b = 3\text{mm}$).

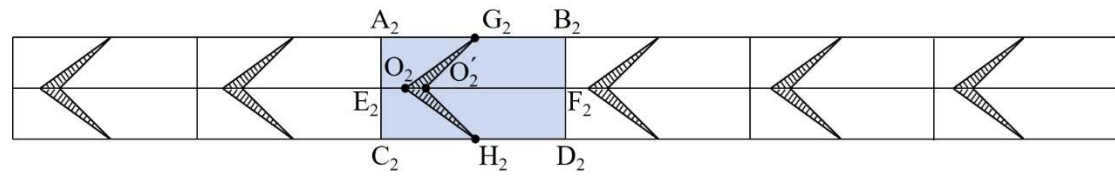


Fig. 12. The flattened view of one hexagonal module with non-rigid deployment mode II.

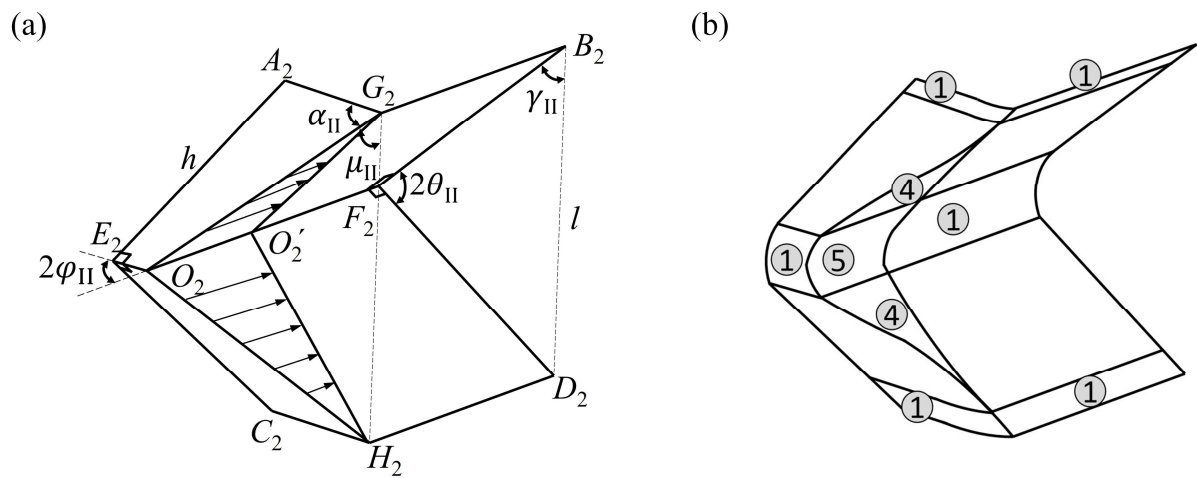


Fig. 13. Geometry (a) and deformation areas (b) of tensile process of basic deployment element with non-rigid deployment mode II.

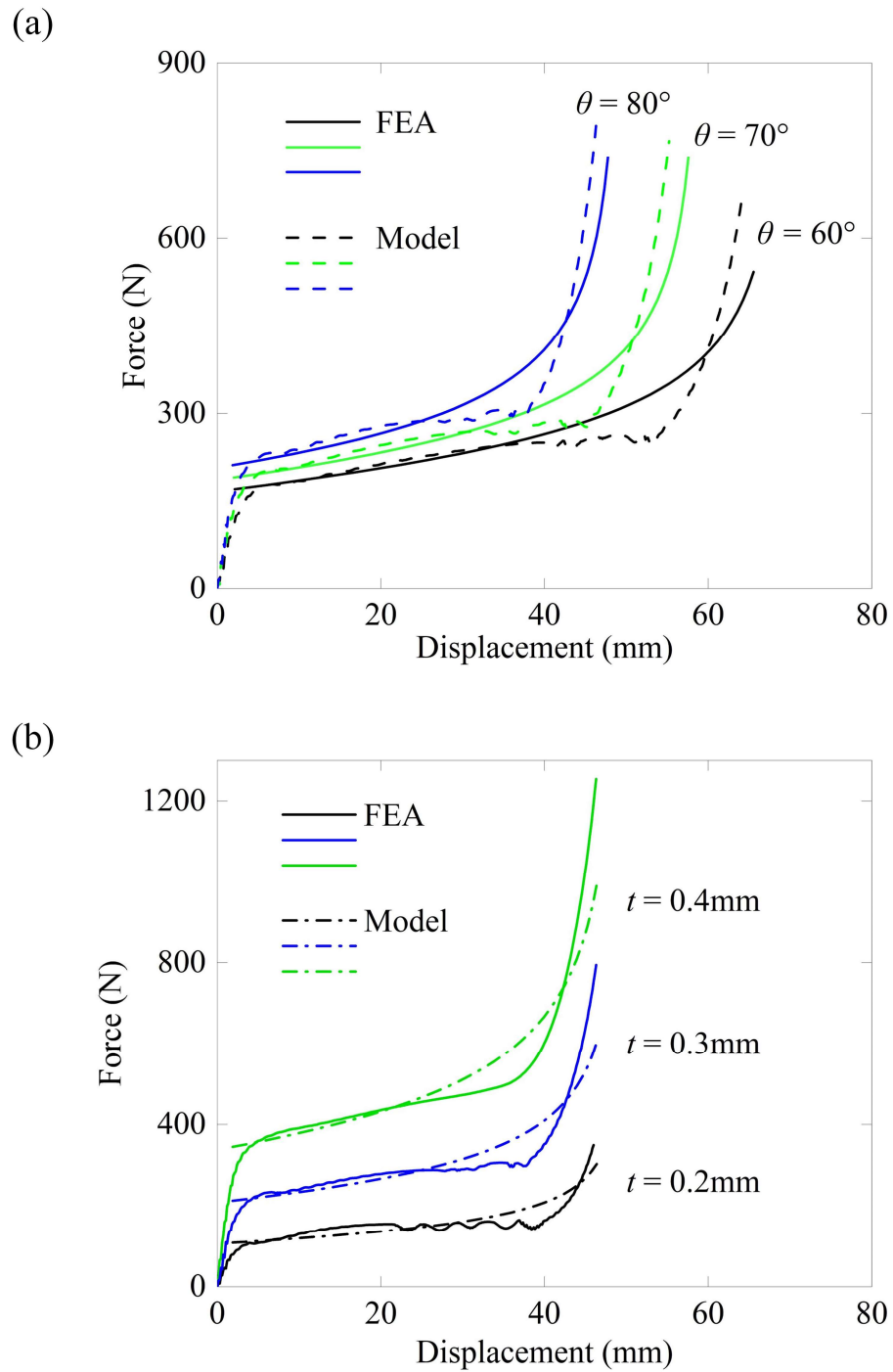


Fig. 14. Force-displacement curves of (a) HEX-60-12-0.3, HEX-70-12-0.3 and HEX-80-12-0.3 with increasing θ , and (b) HEX-80-12-0.2, HEX-80-12-0.3 and HEX-80-12-0.4 with increasing t from FEA and theoretical analysis.

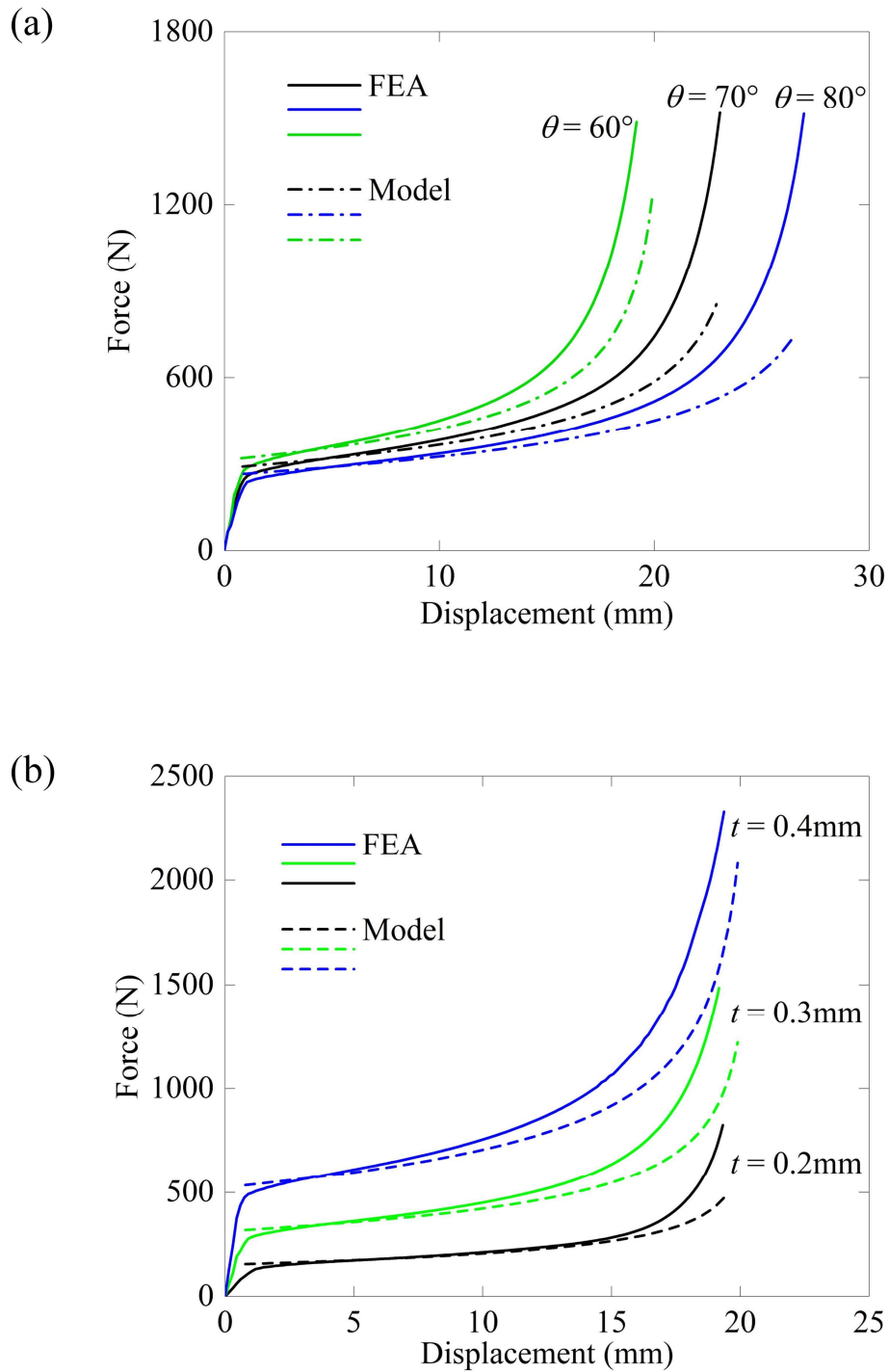


Fig. 15. Force-displacement curves of (a) HEX-60-5-0.3, HEX-70-5-0.3 and HEX-80-5-0.3 with increasing θ and (b) HEX-80-5-0.2, HEX-80-5-0.3 and HEX-80-5-0.4 with increasing t from FEA and theoretical analysis.

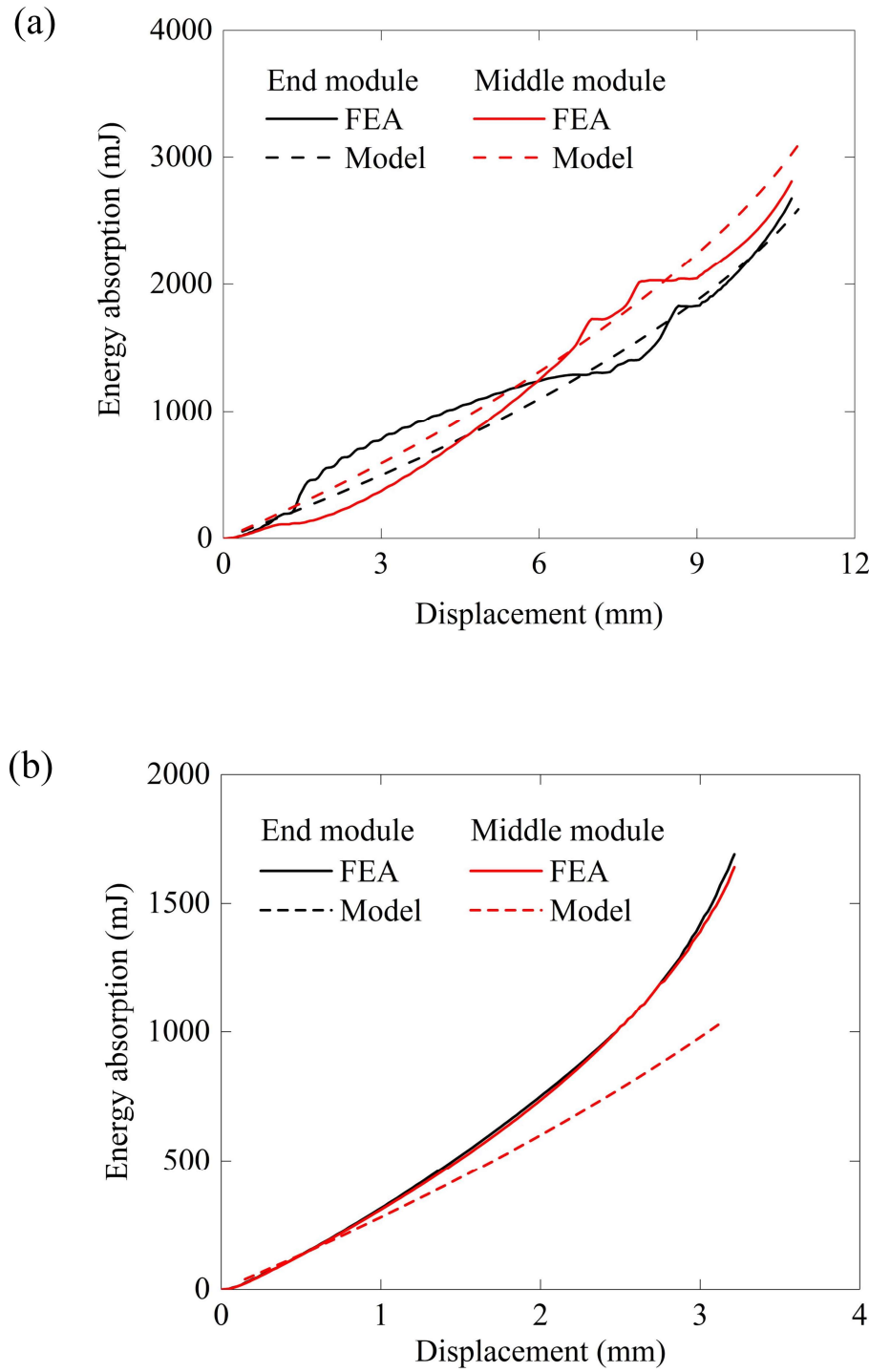


Fig. 16. Comparison of theoretical and numerical energy absorbed by the end module and middle module of (a) HEX-60-12-0.3 deployed in non-rigid mode I and (b) HEX-60-5-0.3 deployed in non-rigid mode II.

Declaration of interests

The authors declare that they have no known competing financial interests or personal relationships that could have appeared to influence the work reported in this paper.

The authors declare the following financial interests/personal relationships which may be considered as potential competing interests: